J. Fluid Mech. (1990), *vol.* 218, *pp.* 265–297
Printed in Great Britain

Transition to turbulence in two-dimensional Poiseuille flow

By JAVIER JIMENEZ

School of Aeronautics, Universidad Politécnica Madrid, P. Cardenal Cisneros 3, 28040 Madrid, Spain *and* IBM Madrid Scientific Centre

(Received 20 February 1989 and in revised form 25 January 1990)

The transition of strictly two-dimensional Poiseuille flow from laminar to chaotic behaviour is studied through full numerical simulation of spatially periodic channels with fairly large longitudinal aspect ratios. The successive bifurcations are studied in detail and their physical mechanism is elucidated. The Liapunov exponents of the flow are measured and shown to be positive at large Reynolds numbers. Isolated, permanent patches of unsteady behaviour, resembling the turbulent 'puffs' observed in circular pipes, are found at low Reynolds numbers and shown to be important for the transition to chaos. The flow exhibits several other phenomena present in natural three-dimensional flows, including wall sweeps, ejections, and intermittency.

1. Introduction

It is generally accepted that turbulence, and, in particular, wall turbulence, is a three-dimensional phenomenon in which processes such as vortex tilting and stretching play important roles. It has also been shown recently that transition to turbulence in wall-bounded flows is intrinsically three-dimensional, even if linear stability theory predicts that two-dimensional disturbances are unstable at lower Reynolds numbers than their three-dimensional counterparts. It appears that these disturbances are indeed the first ones to grow, but that, as soon as their amplitude is finite, they become themselves unstable to much faster three-dimensional secondary instabilities, which quickly become dominant, and lead to turbulent breakdown (Herbert 1983; Orszag & Patera 1983). As such, the original two-dimensional disturbances are never observed in their full-amplitude, nonlinearly saturated, state. The present paper, however, deals with the behaviour of precisely those nonlinear two-dimensional waves in channel flows. We shall show that it is possible to construct, computationally, strictly two-dimensional flows with properties such as chaotic behaviour, ejections and sweeps, large-scale intermittency, and quasi-periodic bursting, all of which are observed in fully turbulent three-dimensional flows. The range of behaviours described in this paper goes from the laminar to the chaotic, and, in that sense, this is a paper on transition. But the emphasis is in the understanding of turbulent flow as such, using a model that has been severely truncated in the spanwise direction, to become actually two-dimensional.

This justifies in part the use of the attribute 'turbulent' for some of the flows encountered in this paper. We shall use it, for lack of a better word, to describe any flow whose time behaviour is chaotic, in the sense of being extremely sensitive to initial conditions, with at least one positive Liapunov exponent. Visual inspection of the corresponding flow fields reveals enough complexity to suggest that many of these flows are also strongly mixing, but that property will not be investigated.

Two-dimensional turbulence has been studied often, even if it is observed experimentally only under very special circumstances. There are several reasons for that, of which perhaps the most important is that it provides a simplified situation in which to study mechanisms that may be relevant to the three-dimensional case. Two-dimensional flows are easier to compute and, above all, much easier to observe than their three-dimensional counterparts, and the mechanisms that act in them can generally be analysed rather fully. The understanding gained from those analyses can sometimes be carried into three dimensions, even if only as an indication of which features are intrinsically three-dimensional, and which ones are not.

Of the many papers dealing with two-dimensional turbulence, few treat statistically stationary self-sustaining flows. Typically, what is studied is the decay of an initially random vorticity distribution. While these studies are interesting, the fact that the only actual attractor of the flow is the rest state complicates the interpretation of what is being observed and prevents the study of such questions as asymptotic behaviour, unpredictability and chaos. All these are characteristic of three-dimensional turbulence, and should be part of any two-dimensional system that tries to model the same phenomena.

It is not easy to find such a system. Most two-dimensional flows are stable, and many which are not, like free shear layers and jets, have integral scales that grow continuously in time. If they are studied in a finite computational, or experimental, box, they eventually hit its boundary, and either decay, or proper boundary conditions have to be provided, whose influence is uncertain. Spatially periodic Poiseuille flow offers a good model in which to look for self-sustaining two-dimensional turbulence. Above a critical Reynolds number, it becomes linearly unstable and develops finite-amplitude two-dimensional waves which eventually saturate (Herbert 1976). Under some circumstances, these nonlinear states become unstable and lead to more complicated motions. In fact, Jiménez (1987, 1989) identified numerically a series of bifurcations into limit cycles, tori and chaos.

It is that flow that we shall study here, through a full numerical simulation of the two-dimensional Navier–Stokes equations. The question of which mechanisms and structures from the two-dimensional channel are relevant to the three-dimensional case will not be discussed directly, and cannot be answered without a careful dynamical analysis of the three-dimensional case which is currently under way and will be the subject of future publications. What we shall do here is to consider the two-dimensional channel as an interesting flow in its own right, and to study it with the same techniques that are commonly used for natural turbulent flows.

The numerical scheme, and, in general, the 'experimental' set-up are described in §2. Sections 3 and 4 present the results of the simulations in short and long computational boxes. The next section discusses the Liapunov exponents of the flow, and the transition to chaos, and §6 presents briefly the average flow quantities, and their relation to three-dimensional channels. Finally some conclusions are offered.

2. The numerical scheme

Poiseuille flow is established between two infinite parallel plates at $y = \pm h$, $h = 1$, with a parabolic laminar equilibrium velocity profile $U(y) = 1 - y^2$. It is governed by the two-dimensional vorticity equation

$$\omega_t + \psi_y \omega_x - \psi_x \omega_y = Re^{-1} \nabla^2 \omega, \tag{1}$$

where ψ is a stream function, generating the velocities $u = \psi_y$, $v = -\psi_x$, and

$$\omega = \nabla^2 \psi \tag{2}$$

is the vorticity. We impose that the volume flux per unit span, $Q = \frac{4}{3}$, remains constant. This is not the only possible choice. Other investigators have used a constant average pressure gradient (Herbert 1976; Saffman 1983; Rozhdestvensky & Simakin 1984), and have discussed the differences between the two cases. When the only solutions considered are those that can be reduced to a steady state in some frame of reference, both conditions are equivalent, since both flux and pressure are constant in time, and the choice reduces to a different parameterization of the solutions, which can be associated to two different Reynolds numbers. For the constant-flux case, $Re_Q = 3Q/4\nu$, and for the constant-pressure one, $Re_p = -h^3 \times (\partial p/\partial x)/2\rho\nu^2$. For uniform laminar Poiseuille flow, both numbers are identical, and, in other statistically stationary cases, they are related through the average vorticity at the wall, ω_w, by

$$Re_p = \tfrac{1}{2} Re_Q \omega_w. \tag{3}$$

Later, we shall find solutions that are unsteady in all frames of reference. For them, the two boundary conditions are intrinsically different, and give rise to different behaviours and stability properties (Saffman 1983; Pugh 1987). Even for asymptotically steady flows, it has been observed often that the approach to equilibrium is different for both boundary conditions, being usually somewhat faster for the constant-flux case. This alone is a strong argument for the use of this boundary condition, in view of the computational cost implied by the long integration times needed for transition calculations. Rodzhdestvensky & Simakin (1984) report unsteady solutions that are *approximately* both constant flux and constant pressure, and imply that they are exactly so. We have not been able to confirm that. Our solutions are always constant flux, but the pressure gradient varies with time in the unsteady case, although the variation is, in some cases, relatively small. The Reynolds number in (1), and in the rest of the paper, is always Re_Q, unless explicitly declared otherwise.

We study the behaviour of periodic disturbances of the form

$$\omega = -2y + \sum_{k=-N}^{N} \Omega_k(y,t)\, e^{ikax}. \tag{4}$$

At low Re, the parabolic profile is stable, but at $Re = 5772$ ($\alpha = 1.02$), it bifurcates into a family of periodic travelling shear waves. This bifurcation is subcritical and can be continued at finite amplitudes to lower Re, until this 'lower branch' turns around near $Re = 2700$, and proceeds towards higher Re, forming an 'upper' branch with larger amplitudes (Herbert 1976). Other wavenumbers enlarge this picture into a continuous, cigar shaped, *neutral* surface with upper and lower sheets, restricted to a narrow range of wavenumbers, $\alpha \approx 1$. The lower sheet is known to be unstable to two-dimensional disturbances, while the upper one is, at least at moderate Re, and for superharmonic perturbations, not only stable but attracting (Zahn *et al.* 1974). Both branches are known to be unstable to three-dimensional perturbations (Orszag & Patera 1983), but those solutions will not be considered here.

To investigate more completely the stability of the 'upper sheet' solutions to two-dimensional disturbances, we integrate numerically the time evolution of the expansion (4) substituted in (1). The numerical scheme is spectral, and is described in the Appendix at the end of this paper. Initially, a small ($\omega' \approx 10^{-5}$) random perturbation with $\alpha = 1$ is added to the laminar flow, and allowed to grow. For

supercritical Reynolds numbers, after a short transient, the growth of the perturbation is exponential up to fairly large amplitudes, agreeing well with the largest eigenvalue of the Orr–Sommerfeld equation. Growth can also be obtained for some subcritical Re by adding stronger initial perturbations to the flow. From the comparison of the predicted and observed linear growth rates, it can be estimated that the numerical error of the integration scheme, at the resolution described below, is equivalent to a shift of 1–2% in Reynolds number (for $Re < 10000$). From later tests on the effect of refining the integration time step and the computational grid, this is also the estimated accuracy of our nonlinear calculations.

For low Reynolds number, the long-term limit of the growing solutions is a uniform steady train of nonlinear waves, lying in the upper sheet of the neutral surface. Once a solution is obtained in this fashion, the behaviour at different Reynolds and wave numbers can be explored by changing the parameters incrementally and using as initial conditions, in each case, the converged solution for a neighbouring point in parameter space. A preliminary exploration was done with $N = 1$.

It is known (Herbert 1976; Pugh 1987) that, for the purpose of mapping the general characteristics of the steady wavetrains in the neutral surface, it is enough to take $N = 4$–8 in the Fourier expansion. We soon found, however, that the characteristics of the unsteady solutions are more sensitive to the number of modes and, especially, that the spatial structure of the flow field is rich enough to need more modes for a proper representation. Since part of our interest is in studying that structure, a comparative study of different spectral resolutions resulted in the choice of 83 Fourier modes ($N = 41$), and 85 Tchebichev modes (128×129 for de-aliasing). For $Re < 10000$, this choice results in Gibbs ripple amplitudes lower than 0.5% in the vorticity fields, and the magnitude of the first Fourier and Tchebichev coefficients neglected in the truncation of the vorticity expansion remains below 10^{-3} and 10^{-4} respectively. Also, when the resolution is decreased or increased by 50%, the variation in the averaged wall stress is less than 0.2%, and that of the r.m.s. value of its temporal oscillation, less than 2%. For comparison, the corresponding variations when the resolution is reduced to 15×65 modes are 0.2% and 30%. On the other hand the qualitative behaviour of the solution, including the first Hopf bifurcation of the nonlinear wavetrain, can be reproduced even with a single Fourier mode ($N = 1$), although the quantitative results are grossly off. At the chosen resolution, the repeatability of the Reynolds-number thresholds between different kinds of unsteady behaviour is below the resolution of our scan, which is about 2%. Since the resolution study was done for Re close to 10000, the computations are probably over-dimensioned for lower Reynolds numbers. However, for consistency, most of the results reported in this paper are computed with the same high resolution. In those cases in which the computational box is enlarged, to contain several longitudinal wavelengths, the number of Fourier modes is increased accordingly.

In all the simulations the time step was kept small enough that the CFL number never exceeded 0.1. Higher CFL numbers tend to generate spurious chaotic behaviour, and this phenomenon was confirmed in at least one occasion by running the same initial conditions on an unrelated numerical code (Kim, Moin & Moser, 1987). This limitation is probably unrelated to numerical instability, since numerical blow-up was seldom observed. However, it is easily seen that the numerical errors involved in the time integration of the shortest spectral modes contain the time step in the form of the CFL number, and with the present second-order scheme are

proportional to the square of the CFL. As a consequence, CFL numbers of order unity, while preserving stability, introduce $O(1)$ errors in the smallest scales presumably leading to the spurious behaviour.

Each flow was run for between 1000 and 6000 time units, or until the evolution of the spatially averaged wall stress had converged to some given temporal behaviour, with stationary low-order statistics. It should be emphasized that those are fairly long times, corresponding, when reduced to flow length using the average mass flow velocity, to channel aspect ratios between 350 and 2000. At the highest Re, the streamwise power spectrum of the vorticity distribution, ω, decays with the wavenumber as k^{-2}, owing to the presence of sharp vorticity sheets. In the core flow, which is essentially inviscid, this decay extends to the computational cutoff after a drop of four decades but, near the walls, there is a viscous range, spanning a decade and a half in wavenumber, in which the drop is much steeper and the total decay correspondingly larger (see spectra in figure 21).

3. Results for short boxes

When the length of the computational box, $2\pi/\alpha$, is chosen so as to contain just one of the primary instability waves, $\alpha \approx 1$, the flow reaches an asymptotic state which is dominated by large vortices of alternating sign, located near the centre of the channel, which induce strong secondary vorticity peaks near the walls. At low enough Reynolds numbers, the resulting wavetrain is steady, and moves downstream with a celerity of the order of $U_c \approx 0.35$–0.4. In a frame of reference moving with that velocity, there are stagnation saddle points near both walls, along whose unstable outgoing branches some of the wall vorticity is carried into the core of the channel, forming sharp vortex sheets which are eventually diffused by viscosity, and which are the most striking characteristics of the flow (figure 1).

When the vorticity equation is averaged over a streamwise wavelength and over time, it reduces to a flux balance across a given y-plane:

$$\langle v\omega\rangle - \frac{1}{Re}\left\langle\frac{\partial\omega}{\partial y}\right\rangle = \text{const.} = \left\langle\frac{\partial p}{\partial x}\right\rangle, \tag{5}$$

where $\langle\ \rangle$ is the averaging operator. The first term in the left-hand side of this equation is the cross-stream convective (Reynolds) vorticity flux, due to the unsteady motion, and the second one is the viscous diffusion flux. The same equation can be written in the form

$$\frac{\partial}{\partial y}\langle vu\rangle - \frac{1}{Re}\left\langle\frac{\partial^2 u}{\partial y^2}\right\rangle = \left\langle\frac{\partial p}{\partial x}\right\rangle, \tag{6}$$

in which the correspondence of the terms is one to one, and which shows that the two vorticity fluxes are just the averaged divergences of the Reynolds and viscous stresses, driven by the streamwise pressure gradient. The two terms in (5) are plotted in figure 2(a), for a steady wave. The results are similar for other cases, both steady and unsteady, and show an active wall layer, in which both fluxes are important, and a more quiescent core. It turns out that this picture is the result of a strong cancellation over time, as shown by figure 2(b), which represents the r.m.s. values of the temporal variation of the two terms in (5), always averaged over a full streamwise period. The scale of this figure is two orders of magnitude larger than the one in figure 2(a), proving that the instantaneous fluxes are much larger than their time averages. This is specially true in the channel core, which now appears as a

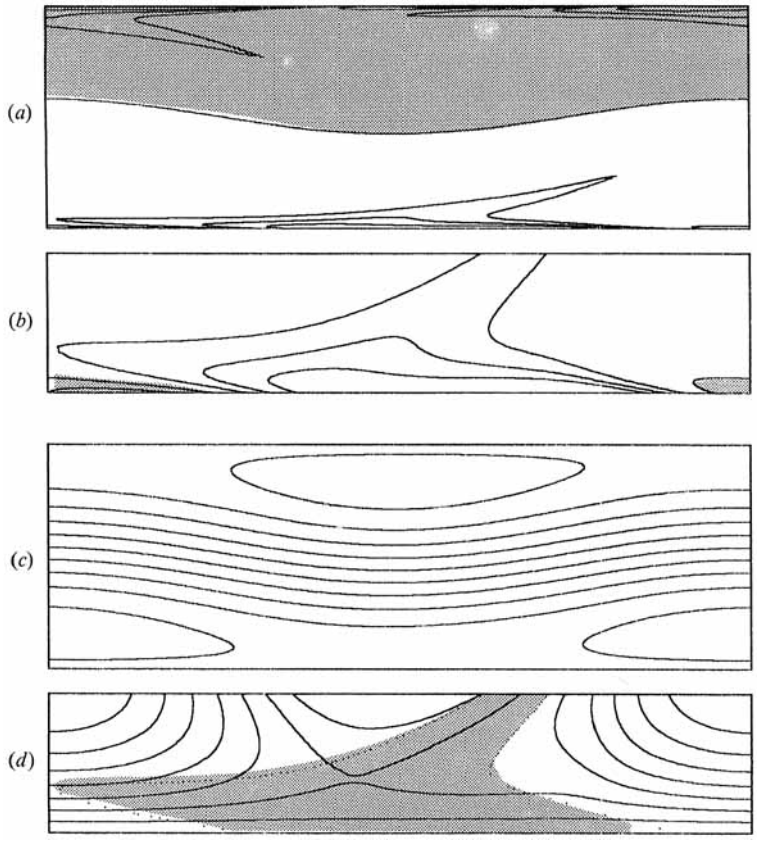

FIGURE 1. Flow maps for a steady equilibrium wavetrain in a short box. $Re = 5000$, $\alpha = 1.0$. Flow from left to right. (*a*, *b*) Vorticity; isolines $\omega = 0, \pm 1.5, \pm 2.5, \pm 3.5$; shaded area is negative; (*a*) full computational box, (*b*) enlargement of lower wall region; vertical extent $y = 0.25$ ($y^+ = 27$). (*c*, *d*) Streamlines; flow and geometry as above. Velocities refer to frame moving with wavetrain, $U_c = 0.353$.

'turbulent' region, dominated by convective fluxes, as opposed to the laminar, viscous, layers near the walls. Defining 'wall' velocity and length scales in the usual way,

$$u_\tau = (\omega_w/Re)^{\frac{1}{2}}, \quad y^+ = y/\delta_\tau = y/(\omega_w Re)^{-\frac{1}{2}}, \tag{7}$$

the thickness of the viscous layers in figure 2(*b*) is about 10–20 wall units, which is of the same order of magnitude as the viscous sublayer in natural three-dimensional plane channels. It will be seen later, however, that the magnitude of the turbulent fluctuations is quite different in these flows from their three-dimensional counterparts.

The uniform steady wavetrains exist down to approximately $Re = 2800$, $\alpha = 1.3$, for a range of wavenumber $\alpha \approx 0.9$–1.6, and have been mapped before by Herbert (1976) and Pugh (1987), although at lower numerical resolution. A map of all our simulations used in the present paper is given in figure 3, where the steady wavetrains are shown as open diamonds. A comparison of our results with those of the previous investigations is difficult, since both authors use Re_p as a parameter, and do not give enough information to relate it to Re_Q. However, Pugh gives some comparable results at the lowest Reynolds numbers, and his boundary for existence

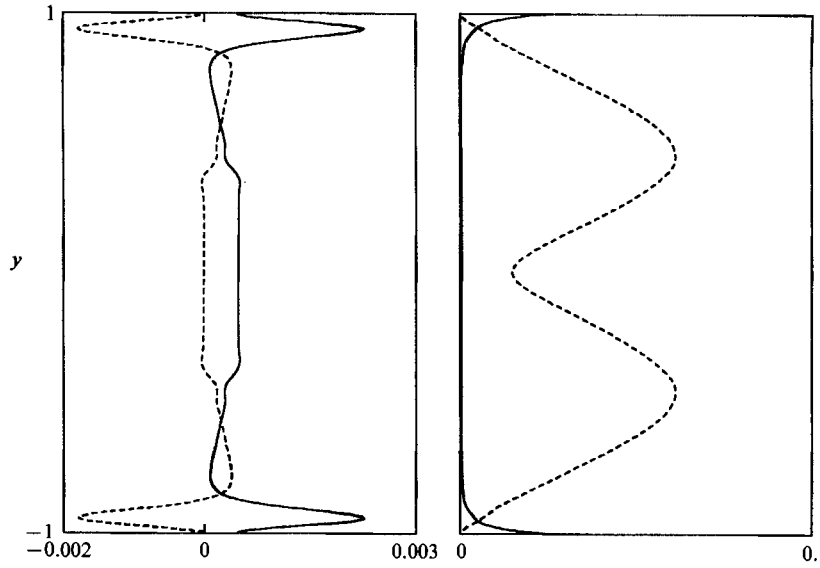

FIGURE 2. Cross-stream viscous (solid) and convective (dashed) vorticity fluxes: (*a*) time average, (*b*) temporal r.m.s. fluctuation. Flow as in figure 1.

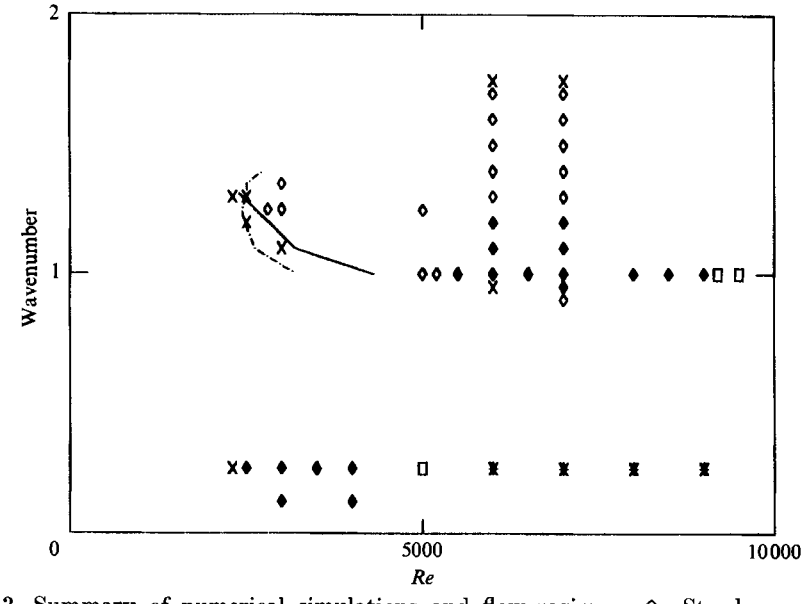

FIGURE 3. Summary of numerical simulations and flow regimes; ◇, Steady wavetrains; ◆, cycles; □, tori; *, chaos; × ; decay to laminar; ——, existence boundary for solutions (Pugh 1987), $N = 2$; –·–·–, $N = 1$.

of the steady solutions is included in the figure. Considering the differences in numerical resolution, the agreement is satisfactory.

Above $Re = 5400$, $\alpha = 1.0$, the steady wavetrains become unstable, and undergo a Hopf supercritical bifurcation into a limit cycle. A convenient variable to describe the temporal evolution of the flow is the instantaneous, space-averaged stress on the lower wall, $\bar{\omega} = \Omega_0(-1, t)$. Below the bifurcation, this quantity is constant, but above it, it oscillates periodically (figure 4*a*), with an amplitude that depends on the

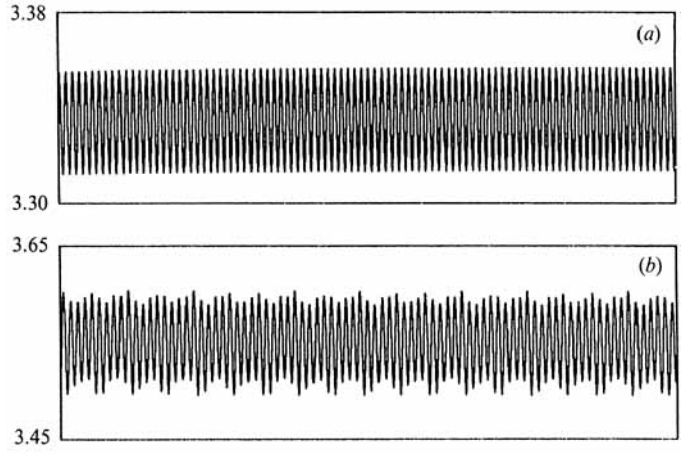

FIGURE 4. Time evolution of averaged vorticity at lower wall, for a short box. (*a*) One-frequency limit cycle; $Re = 7000$, $\alpha = 1.1$; (*b*) two-frequency torus; $Re = 10000$, $\alpha = 1.0$. Total time interval is 1000 in both cases.

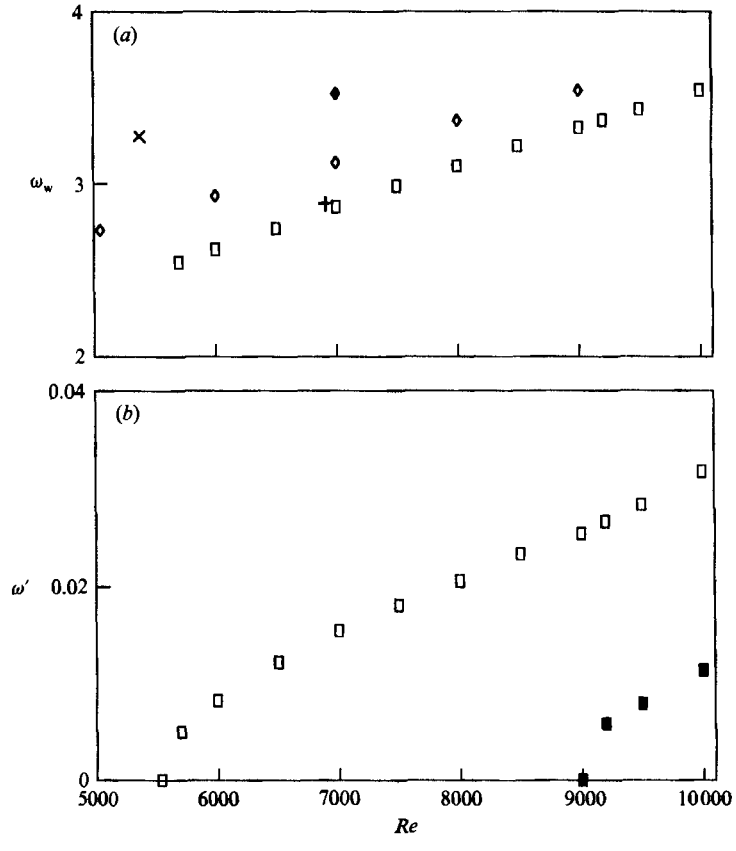

FIGURE 5. Averaged wall vorticity as a function of Reynolds number. (*a*) Time average: □, $\alpha = 1.0$; ◇, $\alpha = 0.25$ (long box); ◆, $\alpha = 0.125$; +, ×, (from Rozhdenvensky & Simakin 1984) $\alpha = 1.0$ and 0.3. (*b*) Temporal fluctuations: □, total r.m.s. fluctuations, cycle or tori; ■, peak-to-peak semi-amplitude fluctuations in tori.

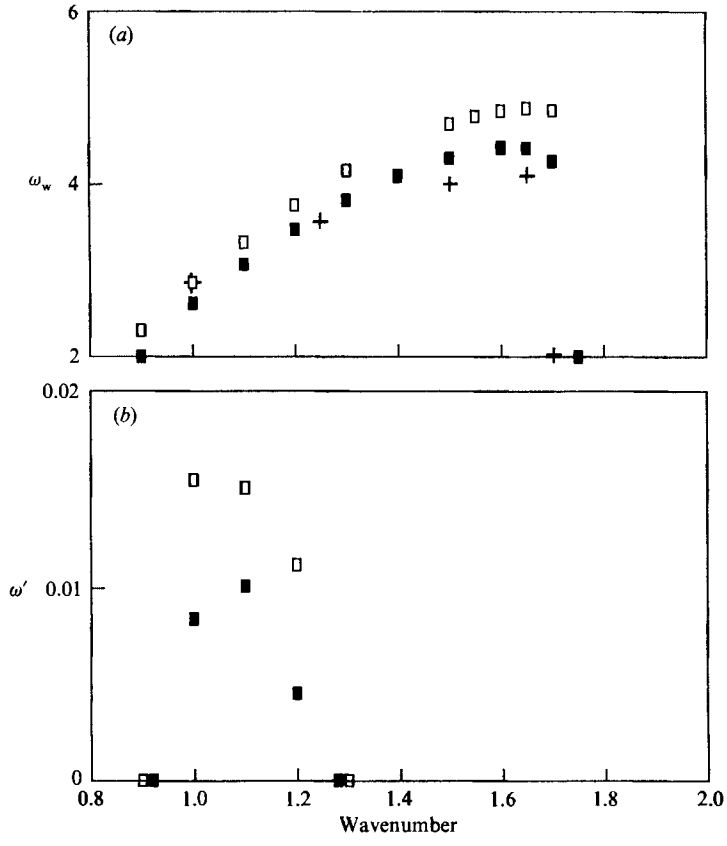

FIGURE 6. Averaged wall vorticity as a function of wavenumber: (*a*) time average, (*b*) r.m.s. fluctuation. ■, $Re = 6000$; □, $Re = 7000$; +, (from Rozhdenvensky & Simakin 1984) $Re_p = 10000$, $Re_Q = 7000$–5000.

Reynolds and wave numbers. At still higher Reynolds number, $Re = 9200$, $\alpha = 1.0$, the solution bifurcates again into a two-frequency torus (figure 4*b*). The ratio of its two oscillation frequencies very close to 5.0 at the bifurcation, suggesting an initial dynamical resonance of the system, and it seems to stay locked at that value for a short range of Reynolds numbers (up to $Re = 9500$), but at $Re = 10000$ the ratio is $T_{\text{long}}/T_{\text{short}} = 4.6$, and does not seem to be expressible as any simple ratio of integer numbers.

At still higher Reynolds numbers, there is some evidence that the temporal behaviour of the oscillation becomes chaotic, but this regime was not mapped carefully, owing to numerical resolution limitations, and also because it was felt that the interesting regimes were those at Reynolds numbers either subcritical to the linear instability threshold, or relatively close to it, in analogy to the situation in three-dimensional turbulent flows. In fact, it will be seen in the next section that the flow in long boxes develops interesting behaviour at fairly low Reynolds numbers.

The dependence of the time-average and fluctuation amplitude of $\bar{\omega}$ on Reynolds and wavenumbers is given in figures 5 and 6, while figures 7 and 8 contain information on oscillation periods and phase velocities. The two first figures include some values of averaged wall vorticity from Rozhdesvensky & Simakin (1984). Although those computations were done at constant average pressure gradient,

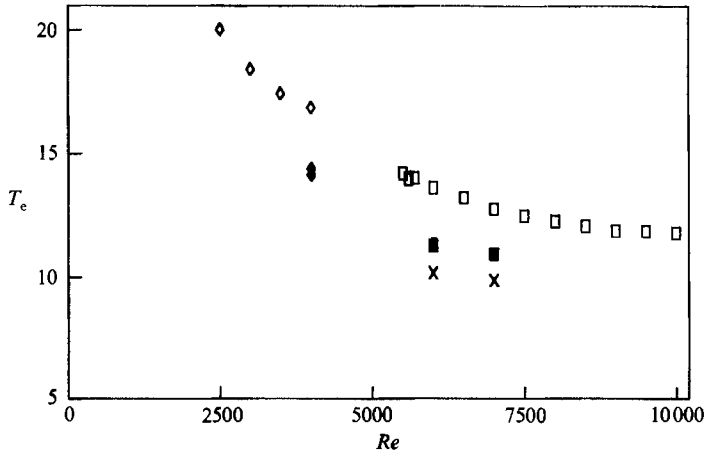

FIGURE 7. Ejection period of limit cycle as a function of Reynolds number: □, $\alpha = 1.0$; ■, $\alpha = 1.1$; ×, $\alpha = 1.2$; ◇ $= 0.25$; ◆, $\alpha = 0.125$.

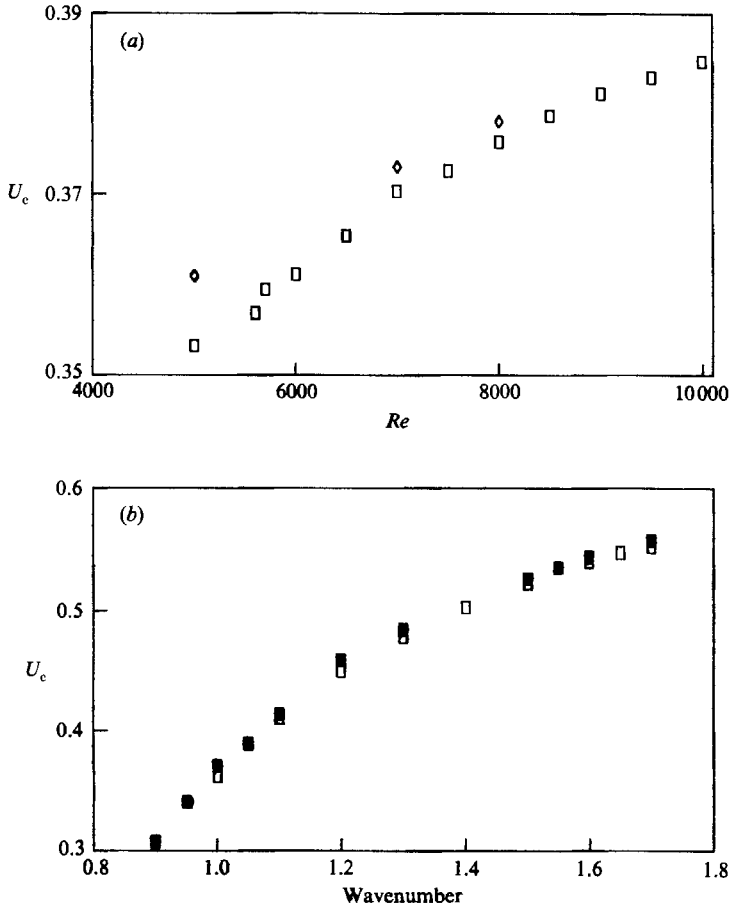

FIGURE 8. Phase velocity of wavetrain. (*a*) Dependence on Reynolds number: □, $\alpha = 1.0$; ◇, $\alpha = 0.25$. (*b*) Dependence on wavenumber: □, $Re = 6000$; ■, $Re = 7000$.

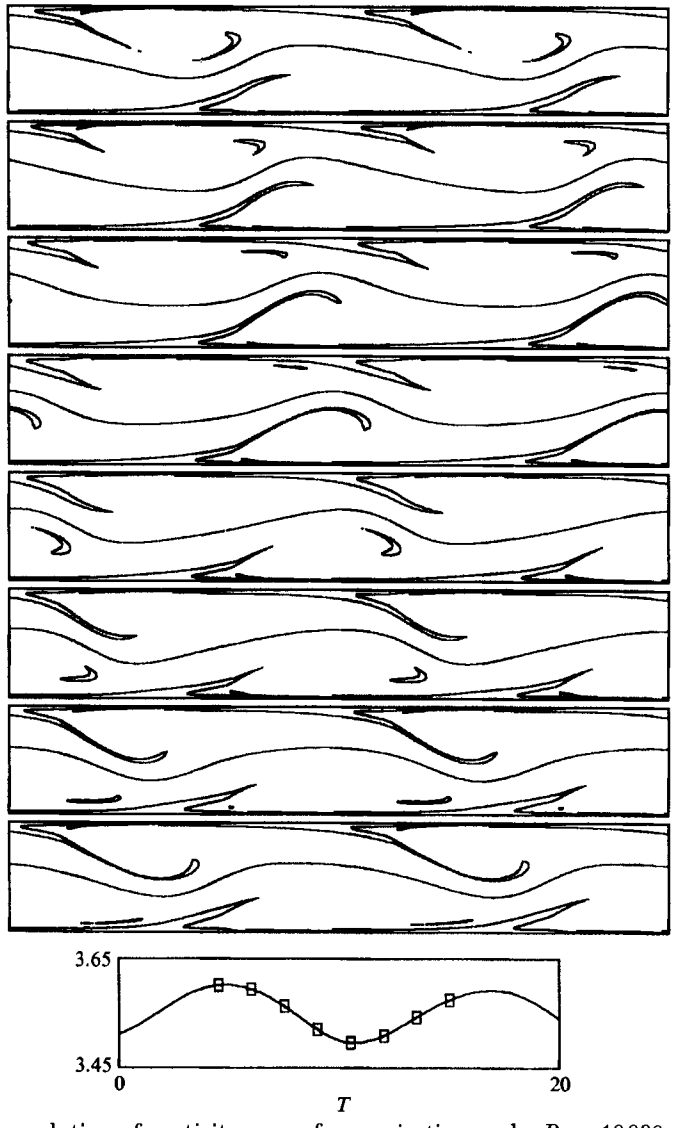

FIGURE 9. Time evolution of vorticity maps for an ejection cycle, $Re = 10000$, $\alpha = 1.0$ (a torus). Flow from left to right and time from top to bottom. Frames are keyed in the wall-stress plot at the bottom. Isolines: $\omega = 0, \pm 1.5$. Each map contains two consecutive computational boxes for clarity.

instead of constant mass flux, the agreement is reasonable, at least in those cases in which the wall vorticity oscillations are small. However, in the single case of a long box ($\alpha = 0.3$) available for comparison, the correspondence is much poorer. Since it is shown below that long boxes are intrinsically unsteady, this is consistent with the idea that, in unsteady cases, the two sets of boundary conditions are not equivalent.

It is clear from these figures that both the limit-cycle and torus bifurcations are supercritical in Reynolds number, with their amplitudes increasing roughly as the square root of the distance to the bifurcation point. It should be stressed that these two bifurcations are different from the original subcritical bifurcation from laminar flow. As described in the previous section, that bifurcation gives rise to a double sheet

of steady-state solutions, whose lower branch is unstable, while the upper one is initially stable, and is the one being investigated here. In fact, in a frame of reference linked to the channel walls, the laminar bifurcation is also Hopf, going from steady laminar flow to a periodic oscillation corresponding to the passing of the Tollmien–Schlichting waves. This first oscillation can be absorbed by an appropriate choice of a moving frame of reference, or, as is the case of the plots in this section, by using space-averaged quantities to characterize the system. It should be realized, however, that to a laboratory observer the steady wavetrains would look like periodic oscillations, and the limit cycles and tori like flows with two and three frequencies. None of the two new bifurcations can be absorbed by a change in the frame of reference.

The nature of the limit cycle is a periodic variation of the amplitude of the whole wavetrain. A time sequence of the flow (figure 9) shows that the vortex sheets originating at one wall eject periodically, injecting extra vorticity in the channel core. Half a period later, the other wall ejects. The cycle can be understood in terms of the transverse velocity induced near the walls by the extra vorticity injected in the channel core by the ejections.

Assuming that a vortex blob is injected in the channel core by an ejection from the lower wall. This small extra vortex is convected down the channel centreline, close to the maximum flow velocity, $U \approx 1$, which is higher than the translation velocity of the wavetrain, $U_c \approx 0.4$. The extra positive vorticity induces an extra transverse velocity away from the top wall, and this 'shadow' outdraft travels with the vortex, just ahead of it, as it is convected downstream. Eventually, the outdraft in the upper wall catches up with the stagnation point which is at the base of the next vortex sheet ahead, and reinforces it for a moment. During this brief period, the amount of negative vorticity pumped by the stagnation point into the upper vortex sheet increases, and the upper wall ejects. The extra negative vortex injected in this way follows the same process as the previous positive one, and eventually generates a new ejection at the lower wall. From this description, the period of the ejection cycle should be of the order of $T = 2\pi/\alpha(U-U_c) \approx 10$, and this is confirmed by the observations (see figure 7).

The vortices generated by the ejections are eventually dissipated by viscosity (actually, after being reingested by the wall layers) and loose their capacity to produce further ejections. At low Reynolds numbers, this happens even before they are able to produce a new ejection in the opposite wall, and the wavetrain is stable. As Re increases, they last long enough to trigger the opposite wall, and an instability appears with a single frequency, while at still higher Re several vortices are present in the flow at the same time and the instability becomes more complicated. Some support for this mechanism is provided by the flows in figure 9, where the ejection in the upper wall roughly coincides with the passing of the vorticity residue from the one in lower wall, and by a similar sequence in figure 12. Additional evidence, in the form of sequences of vorticity fluctuations and near-wall streamlines, is given in Jiménez (1989). Note that, even if in a channel both walls are involved in the ejection cycle, this is not strictly necessary. If a nonlinear equilibrium wavetrain could be sustained in a boundary layer on a single wall, the extra vorticity from one ejection would eventually overtake the next wave, reinforcing the stagnation point and presumably regenerating the cycle. Some preliminary evidence for this mechanism in three-dimensional flows is discussed in Jiménez *et al.* (1988) and Jiménez (1989).

4. Results for long boxes

The previous section deals with the behaviour of the flow when the computational box contains a single wavelength of the nonlinear wavetrain, which is thereby forced to be strictly periodic. In this section, we study boxes long enough to contain several basic wavelengths.

The numerical code is the same as before but the number of Fourier modes is increased so as to maintain the same absolute spatial resolution. Starting from a short box with a established nonlinear wavetrain, $\alpha = 1$, the solution is extended periodically streamwise and perturbed slightly. If the new box is long enough, usually at least four wavelengths ($\alpha = 0.25$), the solution branches into a non-uniform state, whose long-term behaviour depends on the Reynolds number, but which never again approaches a uniform wavetrain.

The investigation was conducted mostly at $\alpha = 0.25$. At low Reynolds numbers, $Re < 5000$, the flow tends to a stable train of wave 'packets'. Each packet is formed from several unsteady waves, each of which is similar to the ejecting Tollmien–Schlichting waves of the short-box simulations, but which differ in amplitude and phase among them. Each group contains a strong, active, leading edge and a slowly decaying trailing edge (figure 10*a*). The permanent character of the configuration was checked by following the flow for more than 1000 time units after it had apparently converged, with total integration times between 3000 and 6000. The resulting history of the averaged wall stress is periodic, with each period corresponding to an individual ejection (figure 11*a*). The phase speed of the individual waves is similar to that of the uniform trains, but the propagation speed of the groups is faster ($U_g \approx 0.75$–0.8). In fact, a movie of the flow shows that each individual wave is triggered by the front of the group, produces a strong ejection, and immediately begins to decay. However, the vorticity from this initial ejection is enough to trigger a new wave in the 'undisturbed' flow in front of itself, propagating the packet in this way (figure 12). In this figure, the frame of reference moves with the phase velocity of individual waves, $U_c = 0.35$, which appear almost stationary in the time sequence, while the group front, marked by the first ejection, moves forward faster. The figure contains both vorticity and Reynolds stress ($-u'v'$) maps. The vorticity tags the evolution of the general structure of the flow, but the stress maps highlight the active locations of the flow field, as distinguished from those in which the wave structure is mainly the result of former activity. The active front, the decaying tail, and the isolated character of the wave groups are clearly visible, and the basic propagation sequence is seen to be an 'incoming' high-stress event, followed by an ejection. Note that this corresponds to the classic *Sweep–ejection* cycle described in three-dimensional turbulent boundary layers and pipes by many investigators (see Cantwell 1981).

Note also that the propagation mechanism seems to be the same as the one discussed in the previous section for uniform wavetrains (figure 9). At the Reynolds numbers at which the steady wave packets exist, this mechanism is subcritical, and the flow needs finite-amplitude perturbations to be triggered. Moreover, the mechanism is not directly self-regenerating since the wall vorticity, once ejected, moves forward, and cannot again influence the vortex sheet from which it originated. In short boxes, the forced spatial periodicity of the flow introduces a feedback that keeps individual waves from decaying, since each ejection feeds on itself through the periodic boundary conditions, and the result is a stable uniform wavetrain. In long boxes each wave depends on the one behind it to be regenerated, and the outcome

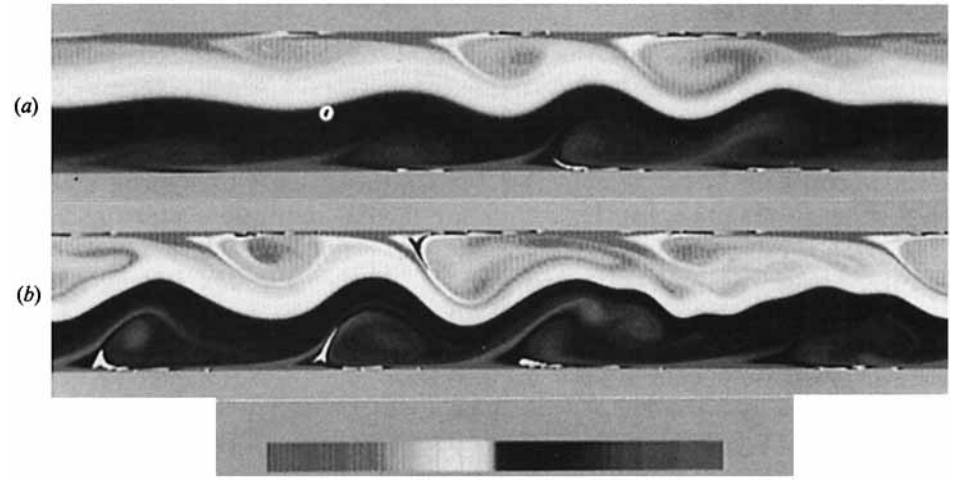

FIGURE 10. Instantaneous vorticity maps for long boxes, $\alpha = 0.25$. The limits of the shading scale, $\omega = \pm 3$, do not reflect the full range of vorticity found in a thin layer near the wall (see figure 17). Vertical scaling; $\times 2$. (*a*) $Re = 4000$, a permanent wave packet. (*b*) $Re = 9000$, a chaotic flow.

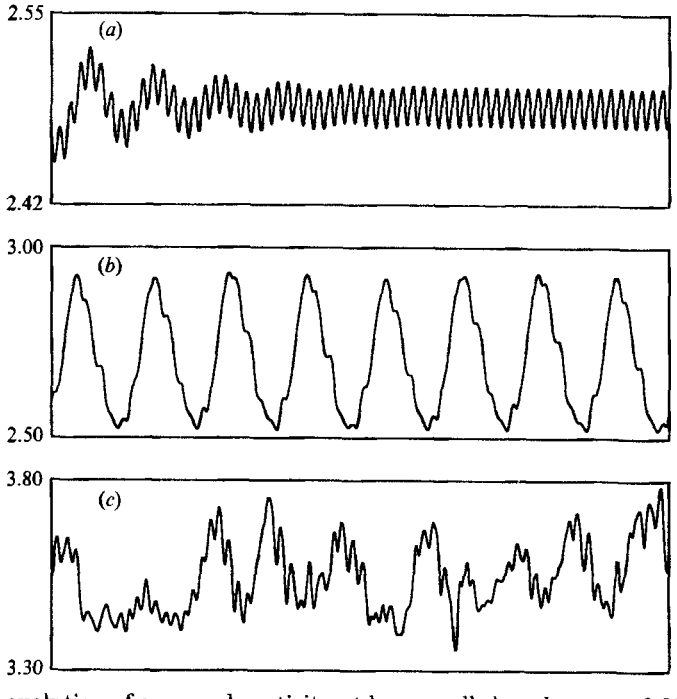

FIGURE 11. Time evolution of averaged vorticity at lower wall; long box, $\alpha = 0.25$. (*a*) Permanent wave packet; $Re = 4000$; (*b*) two-frequency torus, $Re = 5000$; (*c*) chaotic flow, $Re = 9000$. Time interval is 1000 in all cases.

is a gradual decay. It is remarkable that a stable state can be maintained in which what is essentially a single active wave is sustained by continuously reproducing itself on the undisturbed flow in front.

This same information is summarized in figure 13, which is an (x, t) diagram. The

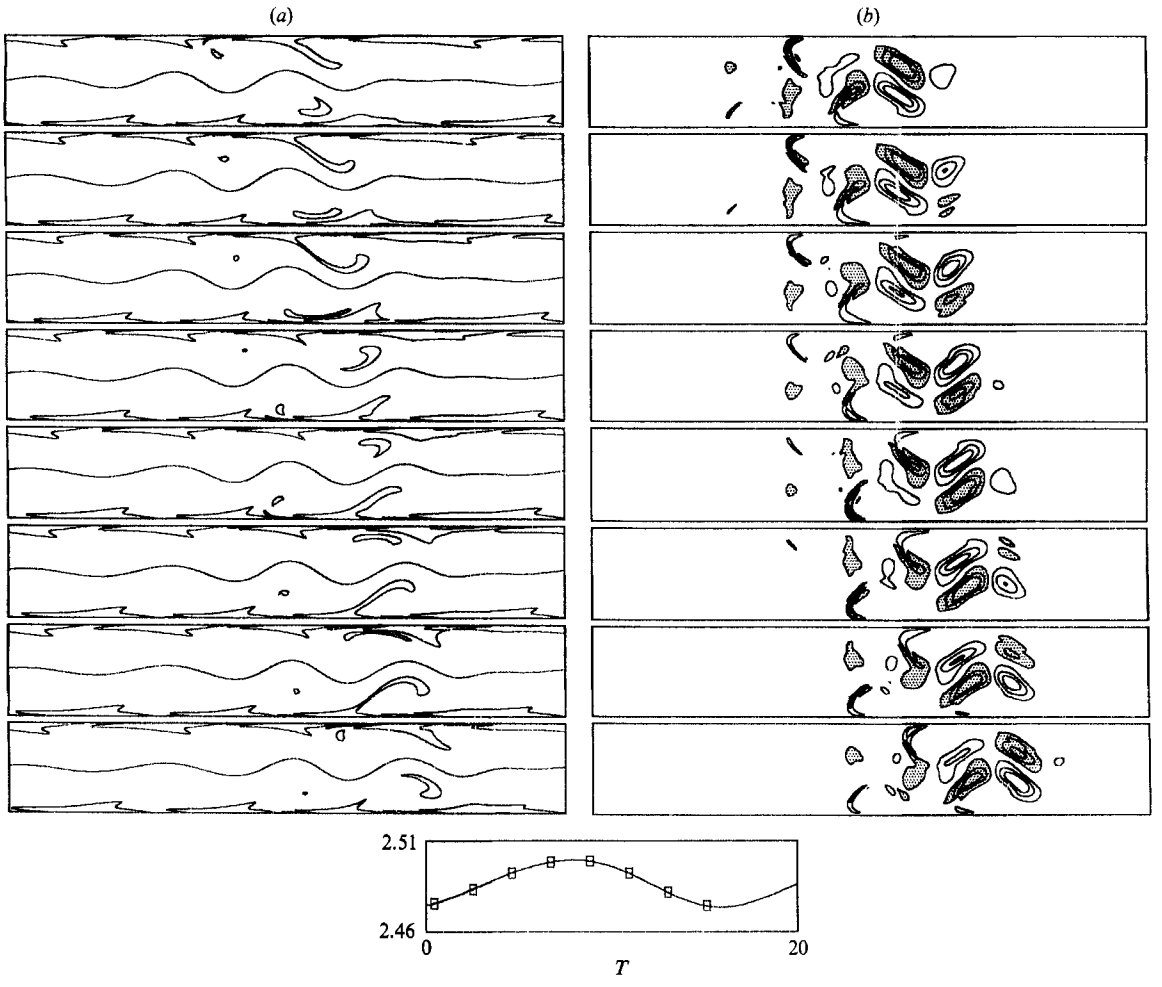

FIGURE 12. Time evolution of flow maps for the propagation cycle of a permanent wave packet, $Re = 4000$, $\alpha = 0.25$. Flow from left to right and time from top to bottom. Frames are keyed to wall stress plot at bottom. (*a*) Vorticity; isolines, $\omega = 0, \pm 1.6$. (*b*) Reynolds stress; isolines, $-u'v' = 0, \pm 0.02, \pm 0.05, \pm 0.08$. Shaded area is below -0.02.

vertical axis is the coordinate $x - U_g t$, increasing upwards, and spans a full streamwise period of the computational box, wrapping on itself; the horizontal axis is time and runs from left to right. Grey levels represent local vorticity at the lower wall, according to the wedge at the left of the figure, in such a way that a local vorticity minimum moving with the group velocity would appear as a horizontal dark strip. Those minima are used to trace the motion of individual Tollmien–Schlichting waves which, since they move at a slower velocity, U_c, appear as downward-sloping dark lines. Grey intensity, or strip width, are an indication of wave amplitude. Each wave is born at the top (and left) of the figure, and drops behind the front of the packet as its amplitude decreases. As this happens, new waves are generated, and the result is a coherent packet whose front moves with the group velocity, U_g. This representation reinforces the impression given by the vorticity maps that a fraction of the length of the channel is essentially laminar, and suggests

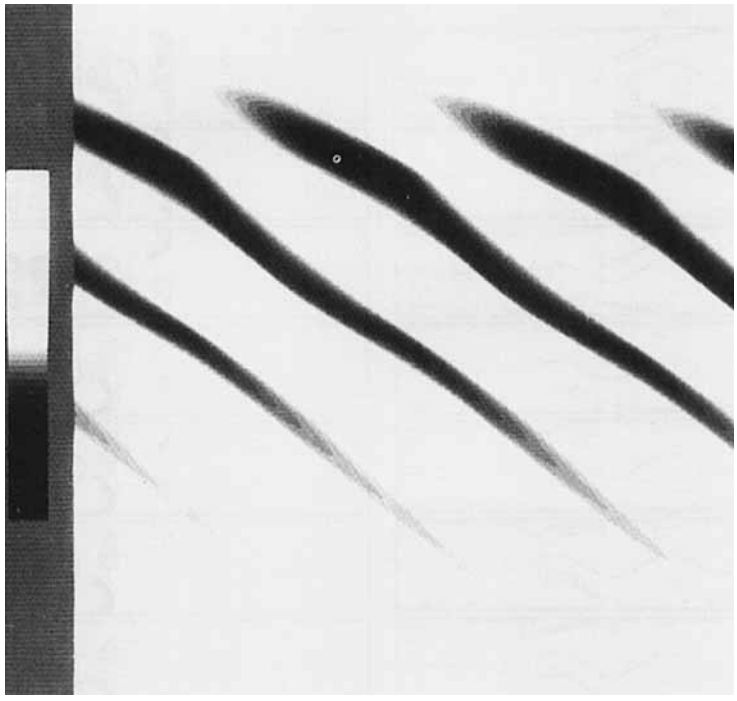

FIGURE 13. (x,t)-diagram of vorticity evolution at the lower wall. Time from left to right and streamwise coordinate from bottom to top. Time interval is 50. Vertical extent is full computational box. $Re = 4000$, $\alpha = 0.25$. Frame of reference moves with convection velocity, $U_c = 0.752$. Grey wedge at left spans $\omega = \pm 16$; dark is negative.

that each wave group can be approximated by a solitary wave packet, propagating by itself in an otherwise laminar channel.

Solitary groups are important features in the solution of systems of equations. In some sense, which will not be explored here in detail, they correspond to homoclinic orbits in dynamical systems. These are orbits starting from a equilibrium state (in this case, laminar flow), and returning to it after a while. A homoclinic orbit itself needs an infinite time to be completed, or an infinitely long channel to develop, and is therefore impossible to observe experimentally. However, it organizes its neighbourhood of the phase space of the solutions of the system of equations, and it can be shown that a small perturbation to a homoclinic orbit generally gives rise to solutions looking roughly like cycles, with periods that are longer the closer the conditions are to the homoclinic solution. It can also be shown that not all of those approximate solutions are necessarily periodic, and that the long-term behaviour of a system in the neighbourhood of a homoclinic orbit will very often look like a chaotic superposition of 'solitary' waves with different separations (see Guckenheimer & Holmes 1983, ch. 6).

Wave packets in long two-dimensional channels, which seem to correspond to the same phenomenon described here, had been obtained before, at low numerical resolution, by Rozhdesvensky & Simakin (1984). Experimentally, solitary permanent packets of turbulent flow have also been observed. The best known examples are 'puffs' in transitional pipes (Wygnanski & Champagne 1973; Wygnanski, Sokolov & Friedman 1975), and spiral turbulence in Taylor–Couette flow (Coles 1965; Van Atta

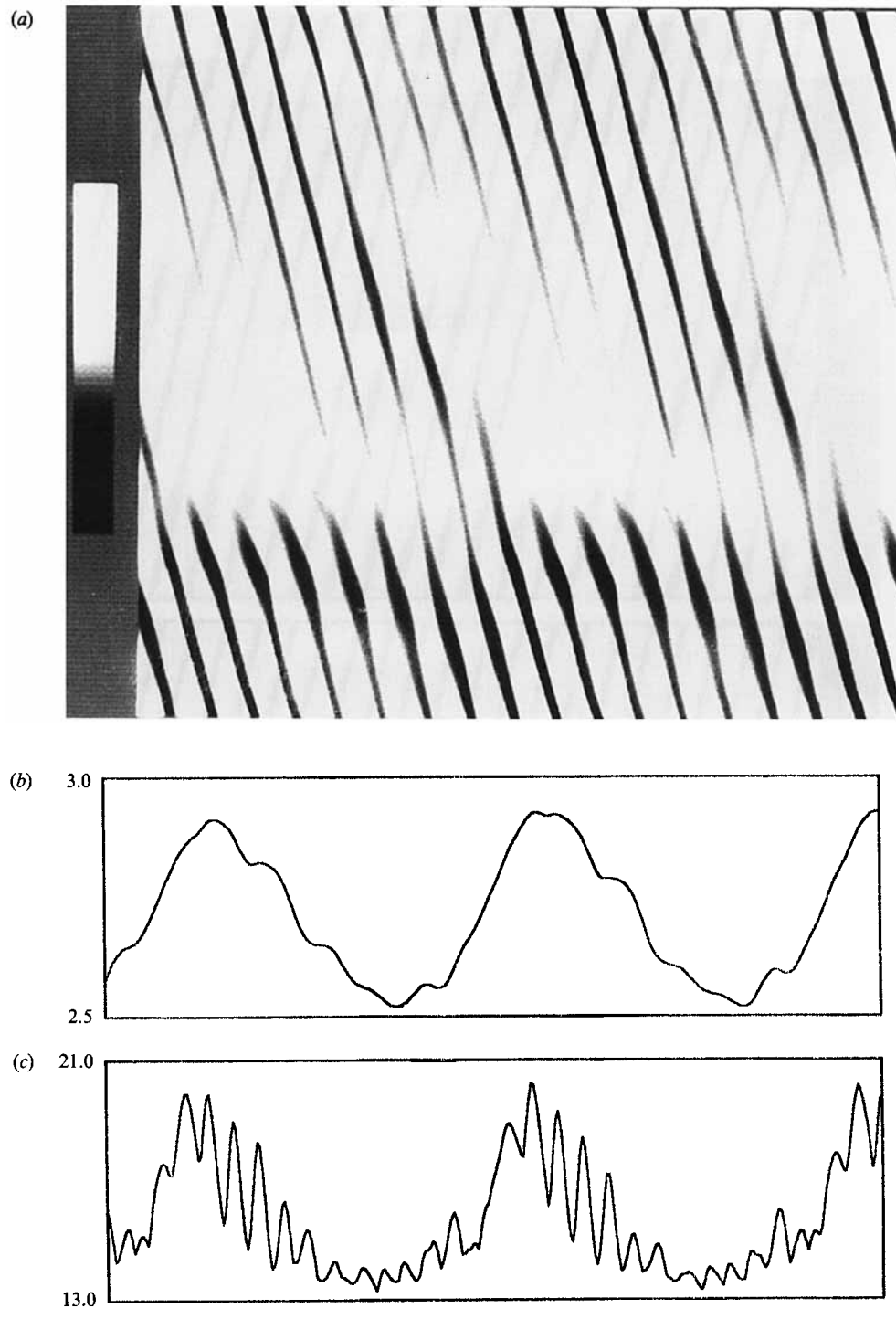

FIGURE 14. $Re = 5000$, $\alpha = 0.25$. (*a*) (x, t)-diagram as in figure 13. Time interval = 290, $U_c = 0.753$. Grey wedge, $\omega = \pm 18$. (*b*) Time evolution of averaged vorticity at lower wall. Timescale is the same as in (*a*). (*c*) Time evolution of maximum absolute value of vorticity over full computational box.

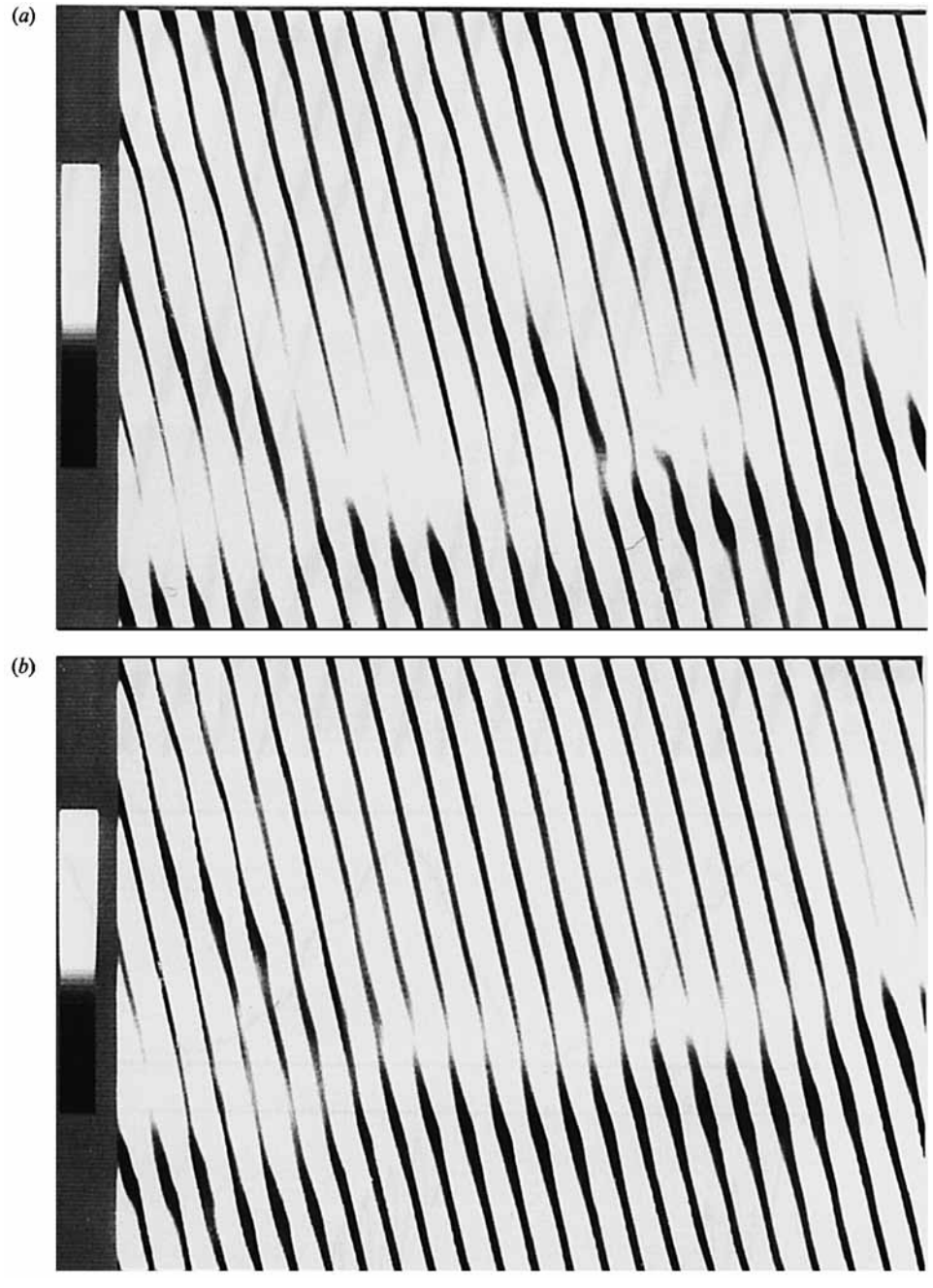

FIGURE 15. as figure 13 but for: (a) $Re = 7000$, $\alpha = 0.25$, $U_c = 0.798$, $\omega = \pm 22$; (b) $Re = 8000$, $\alpha = 0.25$, $U_c = 0.815$, $\alpha = \pm 25$. Time interval = 350 in both cases.

1966; Andereck, Liu & Swinney 1986). In fact, some visualizations of pipe puffs look strikingly similar to those in figures 10 and 16 of this paper (see figure 8 in Bandyopadhyay 1986). Both flows are too different from ours to permit a direct comparison, but it is probably significant that in both cases they occur in subcritical conditions. In fact Pomeau (1986) has argued, on fairly general grounds, that for an

instability front to propagate steadily in a laminar medium, the instability has to be subcritical. His analysis, though, predicts growth both at the front and trailing edge of the perturbation, and does not allow permanent solitary packets without modification.

When the Reynolds number is increased substantially above 5000, the laminar parts of the flow disappear, the flow field gets increasingly disorganized and its temporal behaviour becomes highly unsteady and chaotic (figures 10*b* and 11*c*). An interesting intermediate regime appears between both extremes, in the neighbourhood of $Re = 5000$, $\alpha = 0.25$. Its temporal behaviour is a two-frequency torus, with a slow modulation of the wall vorticity that is almost an order of magnitude larger than the one due to the individual ejections (figure 11*b*).

Its behaviour can be understood from the (x, t)-diagram in figure 14(*a*), which is again keyed to the group velocity. It can be seen that the flow is still basically a wave group, with an active front located near the bottom of the diagram, and a decaying trail that wraps around the top. This tail, however, is unstable, and periodically generates new growing packets (the diagonal patterns crossing the central laminar region), which travel in the wake of the main one at a slower velocity, and are left behind. These new packets are strong enough to grow by themselves and would probably become new independent wave groups if given enough time. In our simulation this never happens, and the secondary groups are engulfed by the front of the primary one once they come around the periodic box. At this point both packets merge and the long cycle of the torus begins again. Figure 14 displays the flow history in the same horizontal timescale as for the (x, t)-diagram, and the two representations can be compared. Figure 14(*b*) is the averaged bottom wall stress that we have used before to summarize history, and it gives an idea of the overall flow activity. Figure 14(*c*) shows the maximum instantaneous absolute value of the vorticity, anywhere in the flow, and characterizes the intensity of the strongest wave. It is seen that, right after the two packets merge, the maximum vorticity increases sharply, probably owing to the triggering of a very strong wave by the vortex patch resulting from the merging. This wave propagates itself in the usual manner, generating new waves ahead of itself, but of decaying magnitude. The decay seems to stabilize somewhat when it reaches a magnitude comparable with the vorticity levels of the solitary packets but, at least in these comparatively short boxes, stops only when it is interrupted by the next packet collision. The average vorticity history follows the same pattern, but its rise is more gradual and precedes the collision because it includes a contribution from the growth of the secondary packet.

This splitting–collision process seems to be the disorganizing mechanism for the flow at higher Reynolds numbers. In fact, some sort of instability of the wave packet is inevitable as the Reynolds number is increased beyond the laminar instability threshold, since the decay of the waves in the tail of the packet assumes the existence of a stable laminar flow towards which to decay. Otherwise, the perturbations of each individual wave would trigger the linear instability. In fact, since the amplitude threshold that is needed to trigger the subcritical *nonlinear* instability becomes smaller as we approach the critical laminar Reynolds number, it can be expected that the splitting process will appear at some subcritical Reynolds number, at which even the small residual perturbation, induced by an ejecting wave on itself, is enough to trigger a new ejection. This is consistent with observation. It will be shown in the next section that the time behaviour of the flow is chaotic for $Re \geqslant 6000$, but the (x, t)-diagrams for these chaotic flows, given in figure 15, show that even in those cases the basic splitting–collapse mechanism is present. The difference seems to be that, at

higher Reynolds number, the secondary group grows more before it is reingested by the front of the primary one, and the details of the reingestion are more disorganised. Splitting of turbulent puffs has been observed in pipes by Wygnanski & Champagne (1973) for a range of Reynolds numbers intermediate between those of equilibrium puffs and those corresponding to growing turbulent slugs, and the subsequent coalescence of puffs to form turbulent slugs is mentioned in the same context by Rubin, Wygnanski & Haritonidis (1980).

From the (x,t)-diagrams, it is possible to define typical phase and group velocities even for apparently chaotic cases. If the mechanism discussed above were true, the main secondary period in these flows, besides the short ejection period of the Tollmien–Schlichting waves, should be given by the length of the box and by the difference between the group velocities of the primary and secondary wave packets, $T_2 = 2\pi/(U_{g1} - U_{g2})\alpha$. For $\alpha = 0.25$, $T_2 \approx 100$, which is close to the 'long' timescale observed in the time traces in figure 11 both for the torus and for the chaotic regimes.

This raises the question of whether this period would increase to infinity for very long boxes, so that the amplitude distribution of the wavetrains will become steady, although not necessarily uniform, in an infinitely long channel. The obvious way to check this hypothesis is to run simulations on longer boxes, but this turns out to be extremely expensive, not only because the number of longitudinal modes becomes larger, but because the relaxation time of the flow increases proportionally to the box length. Nevertheless, we ran a few simulations on a box twice as long as the one described above, $\alpha = 0.125$, although not all of them were continued long enough to make sure that an asymptotic state had been reached. The first experiments were intended to decide whether the permanent wave packets could really be described as solitary waves. These simulations were run as long as necessary, and the result was confirmed. When a $Re = 4000$, $\alpha = 0.25$ wave packet is placed in a box twice as long (with the remainder of the channel left laminar) it retains approximately its initial length, leaving a large part of the channel undisturbed. Actually, the resulting flow is no longer strictly permanent, and the time history acquires a small modulation ($T \approx 200$), whose amplitude is a small fraction of that of the basic oscillation due to the Tollmien–Schlichting ejections. At $Re = 3000$, this modulating disappears (see figure 16*a* for a vorticity map), and the resulting amplitude distribution is really permanent. However, this configuration is not unique. A different initial condition, in which two $\alpha = 0.25$ packets are put in an $\alpha = 0.125$ box, at $Re = 4000$, results into a new permanent amplitude configuration with two unequal packets following each other (figure 16*b*). This configuration was followed for a very long time and, except for the periodic Tollmien–Schlichting ejections, propagates without change.

Some attempts were made to use these two flows as initial conditions at higher Reynolds numbers. At $Re = 5000$, the single soliton immediately begins to oscillate, with an initial period $T \approx 100$, and eventually grows to fill the entire length of the channel with eddies of varying amplitude, which oscillate in an apparently random way but with a characteristic period that grows to be in the neighbourhood of $T \approx 250$. On the other hand, the two-packet solution run at $Re = 7000$ settles, after a long smooth transient, to a fairly regular two-frequency torus, with a long period, $T \approx 200$. Neither of these two simulations was followed to their full asymptotic states. The computer effort involved in each of them, as well as in the permanent cases at lower Reynolds numbers, was in the order of a week of supercomputer time. Still, they suggest that the characteristic long period of the flow scales with the box length, at least in those cases in which the Tollmien–Schlichting waves essentially fill the

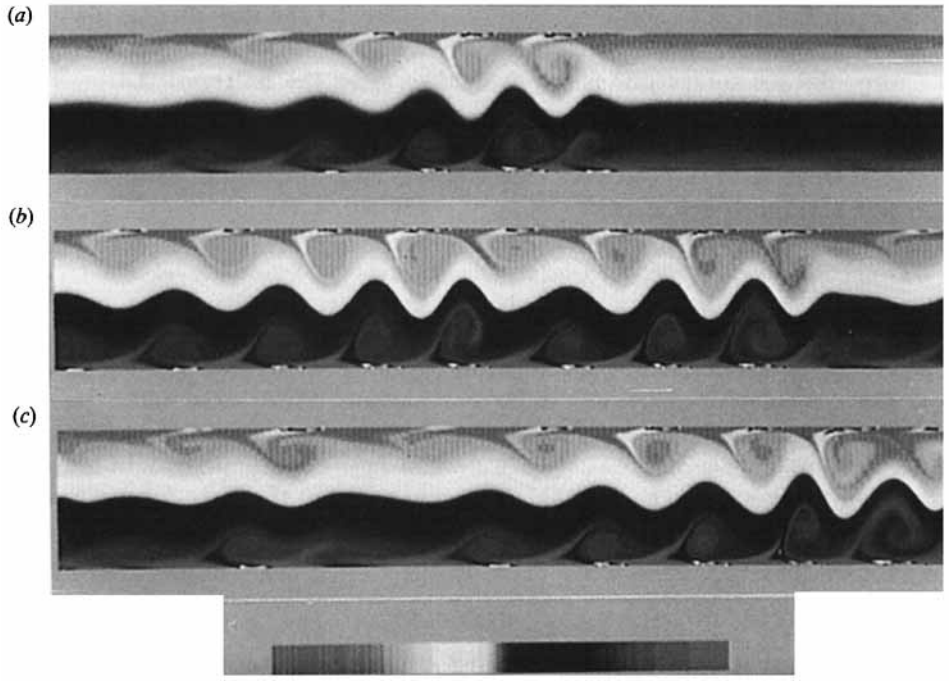

FIGURE 16. Instantaneous vorticity maps for very long boxes, $\alpha = 0.125$. Shading scale as in figure 10. Vertical scaling: $\times 4$. (*a*) An equilibrium wave group at $Re = 3000$. (*b*) An equilibrium two-group configuration at $Re = 4000$. (*c*) A splitting group at $Re = 5000$; the small wave in the left is falling behind the large group in front.

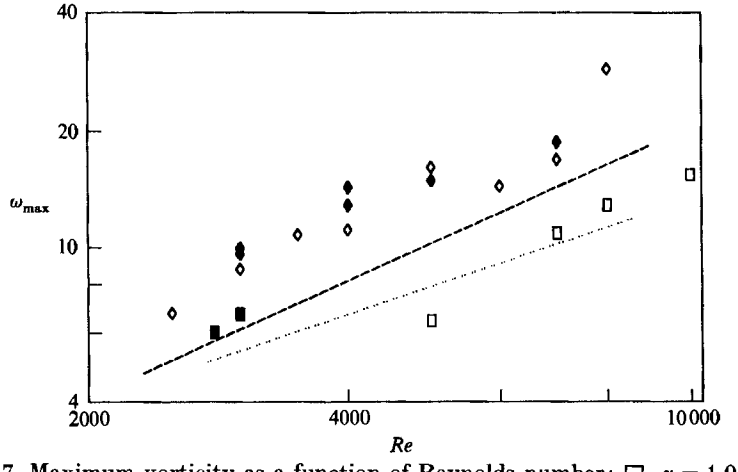

FIGURE 17. Maximum vorticity as a function of Reynolds number: □, $\alpha = 1.0$; ■, $\alpha = 1.25$; ◇, $\alpha = 0.25$; ◆, $\alpha = 0.125$; ----, slope 1.0; ....., 0.75.

channel. The short period of the initial evolution of the soliton at $Re = 5000$ is interesting since it is roughly the same as for the $\alpha = 0.25$ box. In fact, as argued previously, these almost supercritical flows cannot be stable since the laminar flow in the tail of the soliton is unstable to very small perturbations. Thus, a soliton in an infinitely long channel and at a high enough Reynolds number would split spontaneously, on a timescale which is independent of the length of the box. It

appears that, for $Re = 5000$, this scale is approximately $T = 100$ and is observed in the initial evolution of the soliton. In fact, a snapshot of the flow during this initial evolution shows clearly the splitting process (figure 16*c*, the main front is at the right of the figure, the secondary one is much weaker, near the left end). Later, as the laminar portion of the channel disappears, this argument ceases to hold and it is possible to reach steady amplitude distributions of the individually ejecting waves. The long-box experiments described here suggest that this asymptotic state, if it exists, is not a uniform wavetrain.

For long boxes with varying amounts of laminar flow the averaged wall vorticity, which was used in the previous section to characterize the overall level of activity of a given solution, is no longer a good choice. A better quantity is the maximum absolute value of local vorticity, which is also always observed at the wall. Its dependence on Reynolds number is shown in figure 17, which is a log–log plot and contains some results of short boxes for comparison. Since this figure refers to different flow regimes and wavelengths, the results have a large scatter, but they give some idea of the evolution of intensity with Re. The figure contains straight lines that correspond to the laws $\omega \sim Re$ and $Re^{\frac{3}{4}}$. The first one fits the data approximately, while the second, which is also not too far off, is the commonly accepted dependence of wall stress with Reynolds number in fully turbulent three-dimensional channel flows (Dean 1976).

Henshaw, Kreiss & Reyna (1989) have argued that a lengthscale, $\delta_{\min} = (\omega_{\max} Re)^{-\frac{1}{2}}$, can be defined using the maximum local vorticity, in the same way that wall units are defined in terms of the average wall vorticity, and that this is the scale of the smallest features of the turbulent flow field. In free two-dimensional shear flows, the maximum vorticity depends only on the initial conditions, and the smallest scale decreases as $Re^{-\frac{1}{2}}$. In wall-bounded flows, however, figure 17 show that the vorticity increases with Re, and, as a consequence, the corresponding smallest scale behaves like Re^{-1}, imposing a stronger constraint on numerical simulations.

5. Liapunov exponents

A different view of the transition of the flow from order to chaos can be gained through the study of its Liapunov exponents, which are a generalization of the stability eigenvalues of an equilibrium state to the case of evolving systems (see Guckenheimer & Holmes 1983, pp. 280–288, for a rigorous discussion). Consider two different time histories of the same flow, originating from slightly different initial conditions, and define a distance between instantaneous flow configurations. Here, we shall use the L_2 norm of the difference between the full vorticity distributions. As long as the two flow histories stay close enough to each other, their difference satisfies a linearized equation, and it can be shown that, for most systems and for most pairs of initial conditions, the distance between the two solutions behaves, over a sufficiently long time, as $\exp(\lambda t)$. The real number λ is the largest Liapunov exponent (LLE) of the system.

Intuitively, this exponent measures how unstable a given flow history is, and which is the timescale in which the system becomes unpredictable. It is generally true that systems with bounded solutions and a positive LLE are chaotic, since the solutions have to grow exponentially apart while still remaining in the same bounded domain. The magnitude of the LLE, compared to the other timescales in the flow, is a measure of the intensity of the chaos. Note that a zero LLE implies that two solutions will drift apart at most linearly, while a negative one means that they will

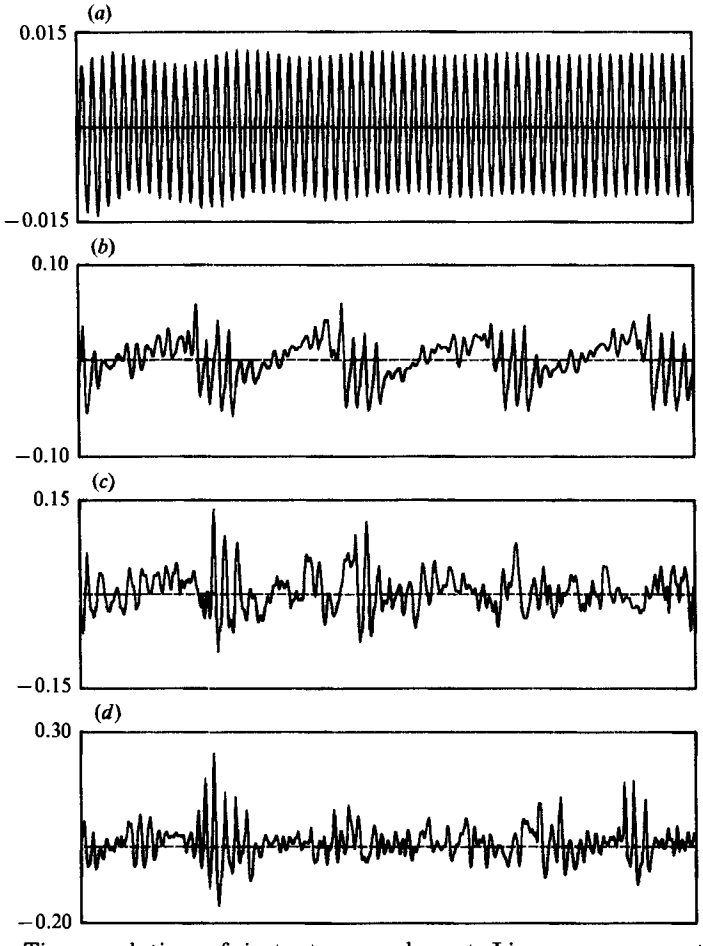

FIGURE 18. Time evolution of instantaneous largest Liapunov exponents, $\alpha = 0.25$. Total time interval in all cases is 500. (*a*) $Re = 4000$, (*b*) 5000, (*c*) 6000, (*d*) 8000. Integration interval, $T = 0.05$.

collapse towards each other. Since all the systems considered here are invariant to a translation in time, their LLE is guaranteed to be at least zero.

An algorithm for computing the LLE of an arbitrary systems is given in Wolf *et al.* (1985) (see also Vastano & Kostelich 1986). The obvious method of starting two neighbouring solutions and watching them grow apart fails numerically because the exponential growth, coupled with the requirement of linearity, requires the use of initial conditions that are too close for the numerical resolution of computers. The answer is to break the calculation into small time intervals, in each of which the separation is allowed to grow a little. After each interval, and before the next one is initiated, the separation is rescaled to a small, linearizable value. Consider an initial condition, $\omega(0)$, and a nearby one $\omega(0)+\omega'(0)$, such that $\|\omega'(0)\| = \epsilon$. After a time T, they evolve into $\omega(T)$ and $\omega(T)+\omega'(T)$, which we can use to compute an estimate of the Liapunov exponent over that first time interval. The next step is to normalize the new separation so that its norm becomes again ϵ. The new initial conditions for the next time interval are $\omega(T)$, and $\omega(T)+\epsilon\omega'(T)/\|\omega'(T)\|$. As the process is repeated, we generate a time series of 'instantaneous' Liapunov exponents,

$$L_n(T) = (1/T)\ln\|\omega'(T)/\epsilon\|, \quad n = 0, 1, \ldots,$$

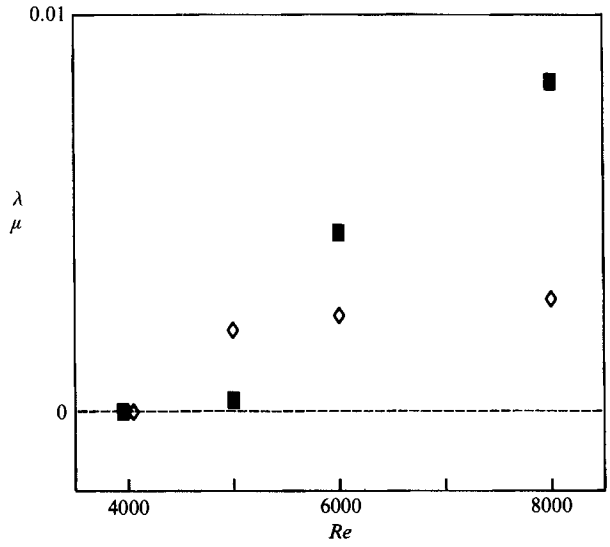

FIGURE 19. Largest Liapunov exponent as a function of Reynolds number, $\alpha = 0.25$: ■, long-term averaged LLE; ◇, reduced variance, μ, for $T = 20$ (see text).

whose long-term average tends to the LLE. The results using an integration interval $T = 0.5$ and after discarding an initial transient of the order of 1000 time units, are shown in figure 18 for several Reynolds numbers and $\alpha = 0.25$. In all cases the calculation of the exponents was started from an already stationary flow ($T \geqslant 2000$). The corresponding long-term averages are given in figure 19. Below $Re = 5000$, the LLE is zero, and the flow is deterministic. Above that value, chaos appears and, for $Re = 8000$, the LLE is fairly large, although still an order of magnitude below the inverse of the ejection period of the flow, $T \approx 13$, which is the basic timescale. This implies that, even at that Reynolds number, the flow still has a substantial deterministic component, in accord with the information of the time histories in figure 11, and of the (x,t)-diagrams in figures 13–15.

In the case of figure 18(a) for $Re = 4000$, the long-term zero average of the L_n is formed by an alternation of stable (negative) and unstable (positive) cycles that cancel out precisely. The frequency of the oscillation is twice the ejection frequency of the Tollmien–Schlichting waves, and a comparison of the time evolution of the Liapunov exponent with simultaneous motion pictures of the vorticity maps shows that the unstable time intervals are associated with the shear-layer ejections from both walls into the core flow, while the stable segments are associated to the viscous collapse of the layers.

Equally deterministic is the case of the torus at $Re = 5000$ in figure 19. Its LLE also vanishes through long-term cancellation of regions of very different character. For a while, the instantaneous exponent rises steadily as the flow becomes more and more unstable, and then collapses suddenly after a few wide oscillations. These oscillating parts of the Liapunov history coincide with the maxima of the averaged wall stress in figure 14(b), and the oscillations themselves correspond to the sharp oscillations in the maximum vorticity shown in figure 14(c). Therefore, the steady increase of the instability corresponds to the growth of the secondary puff in the tail of the primary one, while the collapse of the flow corresponds to the collapse of the instability exponent.

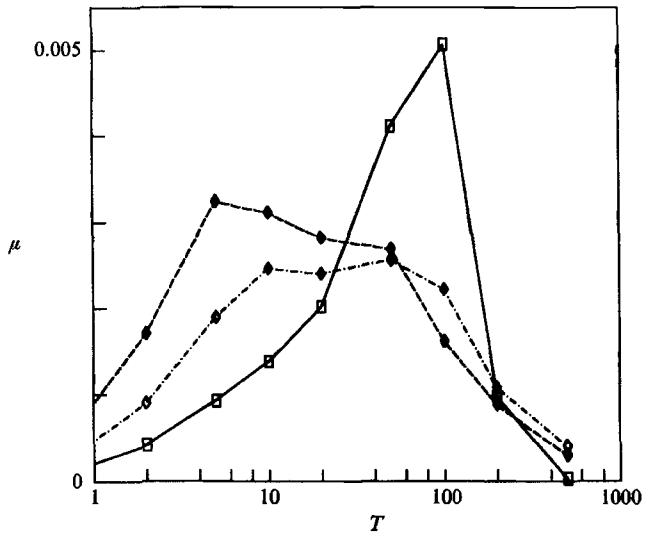

FIGURE 20. Reduced variance, $\mu(T)$, as a function of integration interval, $\alpha = 0.25$: □, $Re = 5000$; ◇, 6000; ◆, 8000.

Benzi *et al.* (1985) suggest that the variance, σ^2, of the sequence of L_n can be used to characterize the temporal intermittency of the flow. For a given system, different sequences can be constructed by varying the integration interval T, and can be simulated by forming running averages from a basic sequence constructed with some short time interval. If the basic process is random enough to satisfy the central-limit theorem, the quantity $\mu = T\sigma^2(T)$ is independent of T, for sufficiently long intervals. In this case, the distribution of the L_n becomes normal, and the long-term behaviour of the divergence of the two trajectories is given solely by the ratio μ/λ. It is shown in that paper that, when $\mu \ll \lambda$, the intermittence can be considered a small perturbation to the chaotic behaviour of the flow, while the opposite is true if μ is of the order or greater than λ.

The evolution of $\mu(T)$ with the integration interval is given in figure 20 for several Reynolds numbers. For the chaotic cases, there is a plateau on which μ is approximately constant, and in which the central-limit assumption seem to hold. It corresponds to integration intervals that are long enough to smooth the oscillations due to the basic ejection cycle, but still short with respect to the timescale of the splitting–collapse process of the wave packets. Taking $T = 20$ as a representative value for this intermediate time-scale, even in the deterministic cases in which no plateau exists, we obtain the values of μ which are given in figure 19. From the above criterion, and from the previous analysis of flow behaviour, it appears that there is a short range between $Re = 5000$ and 6000 in which intermittency may be important, especially in the neighbourhood of the deterministic torus at $Re = 5000$ but that, beyond that range, the chaotic behaviour is well developed and continuous. Since this behaviour is associated to a timescale that averages out the ejection cycle, we confirm the previous conclusion that the appearance of chaos is not directly connected with that cycle but with the splitting and collision of the wave packets.

6. Turbulence statistics

It has been noted often that two-dimensional turbulence, if it exists at all, is not enough to explain the phenomena observed in real three-dimensional turbulent flows. This is also true of two-dimensional Poiseuille flow (Orszag & Patera 1983; Rozhdesvensky & Simakin 1984). Vortex stretching is missing in two dimensions, and the character of turbulence becomes quite different. In particular, the Liapunov exponents of the chaotic behaviour computed in the last section are an order of magnitude smaller than that measured by Keefe, Moin & Kim (1987) for a three-dimensional channel at a somewhat lower Reynolds number. That the two-dimensional transitional instabilities of laminar Poiseuille flow are slower than the three-dimensional ones was known previously (Orszag & Patera 1983). The present evidence implies that this is also true for the fully developed case, although the present Liapunov exponents are already an order of magnitude larger than the viscous eigenvalues, $O(1/Re)$, of the two-dimensional linear instabilities.

Figure 21 contains the streamwise power spectrum of the vorticity field in one of the long-box chaotic flows. The spectrum given by the solid line is averaged across the whole channel, while the dot–dashed one is computed at the wall. The full channel result contains a self-similar range that continues beyond the numerical cutoff, while the near-wall spectrum is dominated by viscosity and decays sharply much sooner. The slope of the 'inertial' range is close to -2, which corresponds to an energy spectrum exponent of $k = -4$. Similar values have been measured in the long-term behaviour of two-dimensional turbulence by Benzi, Patarnello & Santangelo (1987) and Henshaw *et al.* (1989). The second of these papers identifies this decay rate with the formation of coherent structures in the mature flow, in distinction to the $k = -3$ drop-off postulated by the enstrophy cascade theories (Kraichnan 1967; Batchelor 1969), and observed in the early stages of two-dimensional simulations when the energy dissipation of the flow is largest. In the present context, it is clear that the -2 exponent of the enstrophy spectrum is associated with the presence of sharp vortex sheets, which are clearly visible in the flow maps, and which were the essence of the original argument used in Saffman (1971) to predict the $k = -4$ behaviour of the energy spectrum.

Figure 22 contains averaged profiles of the low-order statistical quantities for the same long-box simulation. This is a $Re = 8000$, $\alpha = 0.25$ case, and is the highest Reynolds number for which enough data were stored for a reliable statistic. It has a $Re_\tau = u_\tau h/\nu = 163$, which is reasonably close to that of $Re_\tau = 140$ for the three-dimensional channel in Kim *et al.* (1987). The two flows can be compared directly, and they are very different. The two-dimensional average velocity profile has a thin steep laminar layer near the wall, somewhat reminiscent of the steep profiles of turbulent boundary layers, but is otherwise quite close to the laminar parabolic flow. In particular, it shows an excess velocity at the channel centreline, instead of the velocity defect that is typical of three dimensional turbulent cases. The velocity fluctuation profiles are also different. The two peaks in u' are also found in three dimensions but are much sharper in that case, with maxima close to the edge of the viscous sublayer ($y^+ \approx 10$), while here they are wider and centred further into the channel ($y^+ \approx 60$). They are also stronger in the two-dimensional case, both in absolute value (by a factor of 2) and in wall units (by a factor of 4). The v' profile is also stronger here than in three dimensions, and peaks at the centre, while in natural flows it is usually much flatter.

Figure 22(*c*) shows the Reynolds stress profile, together with the linear total stress

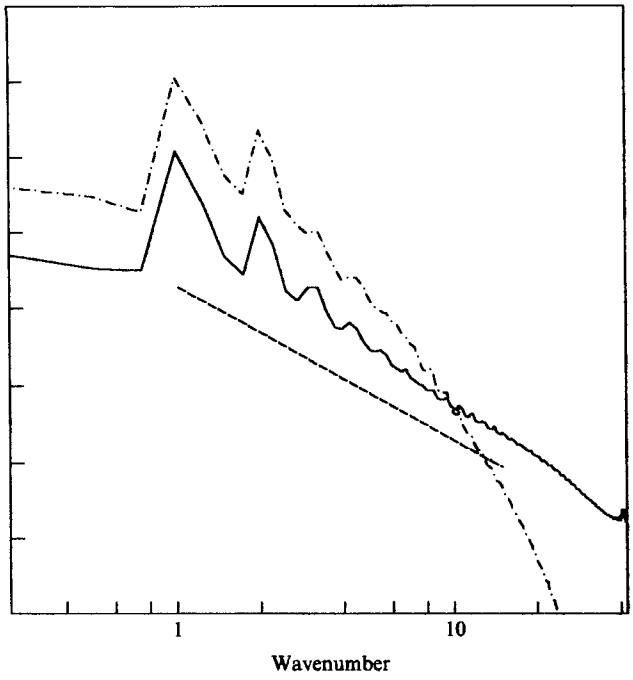

FIGURE 21. Streamwise power spectra of vorticity field, $Re = 8000$, $\alpha = 0.25$. Each division of the vertical axis represents one decade. ——, spectrum integrated over full flow field; –·–·–·–, at wall. Spectra are averaged over 255 dimensionless time units. Dashed straight line has slope -2.

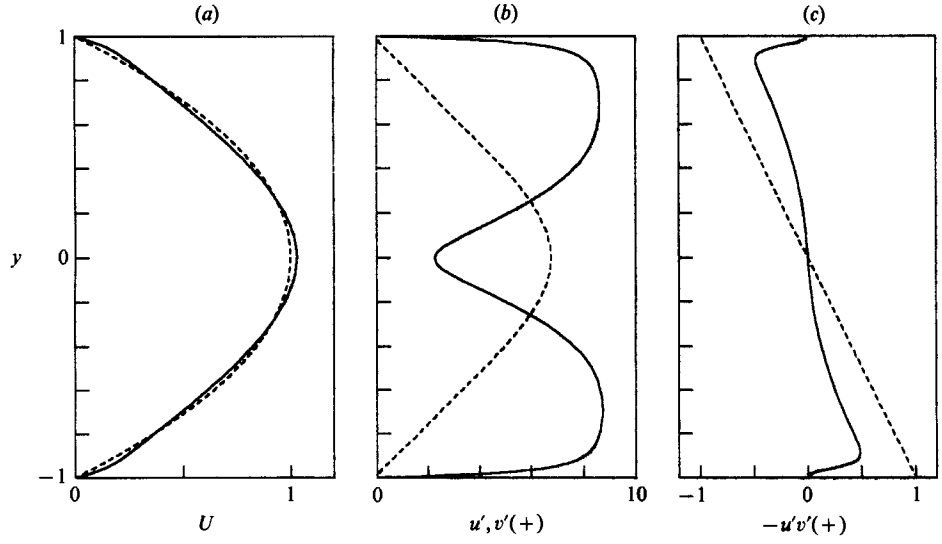

FIGURE 22. $Re = 8000$, $\alpha = 0.25$. (*a*) Average velocity profile; ----, $U = 1 - y^2$; (*b*) Velocity fluctuations: ——, u'; ----, v'. (*c*) Reynolds stress, $-u'v'$; ----, $-u'v' + (1/Re)\partial U/\partial y$. Fluctuating quantities and stress are normalized with the friction velocity, u_τ.

derived from the pressure gradient. The difference between the two quantities is due to viscosity. In fully developed three-dimensional flows, both profiles are very similar to one another outside the viscous layer, while here viscosity retains its importance throughout the channel, at least in an average sense (see discussion for figure 2).

Nevertheless the evolution of the stress profiles with Reynolds number shows a steady evolution from viscous distributions towards more turbulent ones, and it may be that, at higher Re, there are asymptotic states in which Reynolds stresses dominate the full profile. The evolution of the Liapunov exponent in figure 19 also suggests that transition has not been completed at $Re = 8000$.

The dependence on Re of the friction coefficient, which is directly related to the averaged wall vorticity in figure 5, is also different from three dimensions. Expressed in terms of friction velocity, a best fit in the range $Re = 5000$–10000 is $u_\tau = 0.246 Re_Q^{-0.28}$. This corresponds to friction coefficients that are a factor of two smaller than the values recommended by Dean (1976) for fully turbulent three-dimensional channels, and which are described, over a wider range, by $u_\tau = 0.123 Re_Q^{-0.125}$.

In summary, the turbulent flow described here is very different from that observed in three dimensions, although not necessarily weaker, as shown by the velocity fluctuations. It looks as if transition has not been completed at the highest Reynolds numbers studied in this paper, and it is not clear whether a fully turbulent state could be achieved at higher Re. While all the regions of the flow differ significantly from the three-dimensional case, the most striking differences are near the centre of the channel, where the Reynolds stresses are much too low, and the shapes of all the profiles are almost opposite to the natural case. This is not surprising, since it is in this region that the turbulence of a three-dimensional channel is more developed and isotropic, and therefore presumably less similar to the two-dimensional turbulence found here.

7. Discussion and conclusions

As explained in §1, the purpose of this paper was to see whether an equilibrium two-dimensional turbulent flow could be generated and studied. We have seen a series of states of two-dimensional Poiseuille flow that go from the fully laminar to fairly unsteady and chaotic, although there are indications that all those flows are transitional, and that the Reynolds number would have to be increased even further to achieve real, Reynolds-number independent, asymptotic, two-dimensional channel flow. Some indication of the distance to fully developed turbulence is shown by the distance of the Reynolds stress profile to the asymptotic straight-line behaviour (figure 22*c*). This difference decreases with increasing Re, and a rough extrapolation of its evolution points to Reynolds number of the order of 15000–20000 with fairly long boxes, which are outside a reasonable expenditure of present computer resources. That experiment remains a subject for future studies.

In any case, even if asymptotic (two-dimensional) turbulence was not reached, many of the flows studied here are clearly transitional and, in particular, we have shown that they are chaotic, with divergence timescales intermediate between the viscous times, $O(Re)$, and the inertial scale, which turns out to be $T \approx 10$.

The mechanism of the transition to chaos was studied in detail. The basic bifurcation leads to unsteadiness of the sharp vortex sheets ejected from the wall by the nonlinear Tollmien–Schlichting waves, and is mediated by the secondary updrafts induced at the walls by vorticity inhomogeneities in the core of the channel. The original Tollmien–Schlichting waves are actually due to this same mechanism but seem to reach a steady saturation state only in the artificial case of a periodic wavetrain forced by the boundary conditions of short computational boxes. Even in this case, the influence of the ejections from one wave to the one in front of it leads

to a limit-cycle behaviour at high enough Reynolds numbers, and to more complicated tori at still higher Re.

When the condition of spatial periodicity is relaxed by the use of longer computational boxes, the uniform wavetrain turns out to be unstable. No longer able to feed on themselves through the periodic boundary conditions, the individual waves decay, and the flow is maintained only through the propagation of a strong front by means of the induction of a single strong ejection on the fluid ahead of itself. One interesting discovery is that the basic structure of these long boxes, a low Reynolds numbers, is a 'soliton' of ejecting Tollmien–Schlichting waves, with a strong propagating front and a decaying trail, and with much of the flow remaining essentially laminar. Traces of this structure can be found at higher Reynolds numbers, in which case it becomes unstable and splits into secondary groups, which later collide among themselves and are the main agents of the appearance of chaos. There are indications that the frequency of the collisions decreases for very long boxes, and that the resulting flows may be more ordered, even if still unsteady. It is not known whether a infinitely long channel would sustain an essentially stationary train of solitons at all Reynolds numbers. Such a train, containing two back-to-back unequal wave groups, was found in the case of a very long box at $Re = 4000$, but this same solution when carried to a higher Re began to oscillate spontaneously. However, the possibility that the chaos is an artefact of the finite box size and would disappear for very long boxes cannot be discounted completely by the present experiment. On the other hand, the relaxation time needed by the flow to reach its asymptotic state seems to be also proportional to the box length, and it is probable that the steady state, if it is ever reached for an infinite channel, will take such long times as to be of no observational importance. As it is now, the time needed by the flow to settle to a steady soliton at $Re = 4000$ in an $\alpha = 0.125$ box is $T = 3000$, which correspond to about 1000 channel 'diameters' at the mass flux velocity. Some of the simulations at higher Reynolds numbers, even with much shorter boxes, took twice as long to converge to their asymptotic behaviour.

The phenomena of soliton generation, splitting and collision, with the consequent generation of turbulence, bring to mind the classical descriptions of transition in circular pipes and perhaps also the phenomenology of spiral turbulence in Taylor–Couette flow, even if we have shown in the last section that the details of the two-dimensional turbulence described here are very different from those of the three-dimensional case. It is possible that the underlying similarity may not be so much the detailed mechanism of turbulence production, but a more general characteristic of the saturated states of subcritical instabilities. The fact that many of the asymptotic states presented here can be described as trains of unsteady waves with slowly varying amplitudes (and maybe phases) suggests that they may be described by some simplified amplitude equation, and that this may be the unifying link accounting for the similarities between the different flows. The observation by Pomeau (1986) cited above on the question of fronts and subcritical instabilities was made in this amplitude-equation context. It is known that, under some circumstances, the amplitude of the Tollmien–Schlichting waves in Poiseuille flow satisfies the Ginsburg–Landau equation (Stewartson & Stuart 1971) and, although no stable solitary wave solution to this equation is known, it has been shown recently that the inclusion of a quintic nonlinearity leads to the appearance of solitary wave packets, under subcritical conditions, that are not only stable but attracting (Thual & Fauve 1988). These packets do not undergo the processes of splitting and

coalescence that seem to characterize transition in plane channels and pipes, but there are indications that the addition of simple, and physically meaningful, extra dispersive terms to the equation is enough to produce these phenomena. This matter is now under active investigation, and the result will be the subject of future publications.

In summary, we have presented the phenomenology of transition in a two-dimensional flow, which is, by necessity, very different from its three-dimensional counterpart studied up to now. The fact that so many similarities appeared was a surprise. Some of them, like the presence of velocity sweeps, and vorticity ejections from the wall, both in two- and three-dimensional channels, can be attributed to similar physical mechanisms in both flows, but others, like intermittency, solitary turbulent patches, and the route to chaos itself, may be more fundamental and may correspond to general properties of subcritical instabilities. The availability of a well-characterized new model that exhibits all these phenomena should aid in the understanding of what is intrinsic and what is accessory to the different aspects of turbulence.

This work was supported in part by a grant of computer time at the IBM-3090 of the CIEMAT Centre at Madrid, and by the Joint Spain–US Committee for Scientific and Technological Cooperation, under contract CCA-8510/057, as well as by the IBM Madrid Scientific Centre. The simulations for the longest boxes were made possible by additional grants of computer time at the IBM ECSEC Centre in Rome and at the IBM T. J. Watson Research Centre at Yorktown Heights, NY. The help of M. Briscolini and Dr J. A. Zufiria in those two centres is gratefully acknowledged. W. Henshaw and A. Norton, at Yorktown Heights, helped with the preparation of a video of the vorticity maps that helped immeasurably in the interpretation of some flows. L. Keefe and P. Moin, of the Centre for Turbulence Research, run some calculations to check the accuracy of the numerical scheme, and made many valuable suggestions. R. Benzi and H. O. Kreiss made me aware of their respective papers as referenced in the text. I have benefited from discussions with P. Huerre and Y. Pomeau regarding amplitude equations and subcritical instabilities, and with P. G. Saffman on much about the general behaviour of Poiseuille flow.

Appendix

The numerical procedure uses Tchebichev expansions in y for each of the coefficients of the expansion (4), and a fully de-aliased collocation approximation, in both x and y, for the nonlinear terms of equation (1). The time integration is a split-step finite-difference scheme, and the boundary conditions are applied at the end of the last partial step using an influence matrix technique. We define perturbation velocities with respect to the parabolic profile as $\psi_y = u = U(y) + \hat{u}$ and $\psi_x = -v$. The resulting evolution equation for each of the Fourier components in (4) is

$$\frac{\partial \Omega_k}{\partial t} + \left[\mathrm{i}k\alpha U(y) + \frac{k^2\alpha^2}{Re} \right] \Omega_k = -\left[\hat{u}\frac{\partial \omega}{\partial x} + v\frac{\partial \omega}{\partial y} \right]_k + \frac{1}{Re}\frac{\partial^2 \Omega_k}{\partial y^2}. \tag{A 1}$$

The bracket on the right-hand side represents the kth Fourier components of the perturbation convective term, and it is computed pseudo-spectrally with full de-aliasing by using the $\frac{3}{2}$ rule (Orzsag 1971). The rest of the equation is handled directly in spectral representation. The streamwise viscous diffusion and the convection due

to the laminar profile are left in the left-hand side of (A 1), and integrated exactly, helping to reduce the CFL restriction. The result is

$$\Omega_k(t+\Delta t) = \mathrm{e}^{-\Delta t S_k}\left[\Omega_k(t)+\int_0^{\Delta t}\mathrm{e}^{\xi S_k}F_k(t+\xi)\,\mathrm{d}\xi\right]+\frac{1}{Re}\int_0^{\Delta t}\mathrm{e}^{(\xi-\Delta t)S_k}\frac{\partial^2\Omega_k(t+\xi)}{\partial y^2}\mathrm{d}\xi, \tag{A 2}$$

where
$$S_k(y) = \mathrm{i}k\alpha U(y)+k^2\alpha^2/Re, \quad F_k(y,t) = \left[\hat{u}\frac{\partial\omega}{\partial x}+v\frac{\partial\omega}{\partial y}\right]_k. \tag{A 3a,b}$$

The first integral in the right-hand side of (A 2) is computed by a second-order Adams–Bashforth formula, while the second one is approximated by simple reverse Euler. The result can be written as a split-step scheme

$$\tilde{\Omega}_k(t) = \mathrm{e}^{-\Delta t S_k}\left[\Omega_k(t)+\int_0^{\Delta t}\mathrm{e}^{\xi S_k}F_k(t+\xi)\,\mathrm{d}\xi\right], \tag{A 4a}$$

$$\Omega_k(t+\Delta t)-\frac{\Delta t}{Re}\frac{\partial^2\Omega_k(t+\Delta t)}{\partial y^2} = \tilde{\Omega}_k(t). \tag{A 4b}$$

The first step is fully explicit, while the second one is a Poisson solver, which is easily handled in the Tchebichev representation (Gottlieb & Orszag 1977). The same is true of the solution of equation (2), which is needed to close the time step, and which results in

$$\frac{\partial^2\psi_k(t+\Delta t)}{\partial y^2}-k^2\alpha^2\psi_k(t+\Delta t) = \Omega_k(t+\Delta t), \tag{A 5}$$

where the $\psi_k(y)$ are coefficients of a Fourier expansion for the stream function, similar to (4).

The boundary conditions are

$$\frac{\partial\psi_k}{\partial y}(\pm 1) = 0, \quad \psi_k(\pm 1) = 0. \tag{A 6a,b}$$

They are applied using a Tchebichev tau method. Two of them can be used directly when solving equation (A 5), but the other two have to be applied to the vorticity, even if they are expressed in terms of the stream function. This is done using an influence matrix technique. The partial steps (A 4*b*) and (A 5) are applied three times for each time step, in each case satisfying the conditions (A 6*a*), but with a different value for $\tilde{\Omega}_k$. The first application, whose result we will call Ω_{k0}, ψ_{k0}, uses as a starting point the result of (A 4*a*). The other two, which are equivalent to the tau approximation, are started with $\tilde{\Omega}_{k1} = T_M(y)$, and $\Omega_{k2} = T_{M-1}(y)$, which are the two highest-order Tchebichev polynomials used in the expansions for the vorticity components. The final result for $t+\Delta t$ is formed as the linear combination

$$\Omega_k(t+\Delta t) = \Omega_{k0}(t+\Delta t)+\beta_1\Omega_{k1}+\beta_2\Omega_{k2},$$
$$\psi_k(t+\Delta t) = \psi_{k0}(t+\Delta t)+\beta_1\psi_{k1}+\beta_2\psi_{k2},$$

where the coefficients are chosen so that the final stream function satisfies also the conditions (A 6*b*). Note that the vectors Ω_{k1}, Ωk_2, and the corresponding stream functions, are constant and only have to be computed once at the beginning of the integration. Fairly similar methods have been used by Deville, Kleiser & Montigny-Rannou (1984) for a Stokes problem, and by Kim *et al.* (1987), for a problem similar to the one discussed here.

REFERENCES

ANDERECK, C. D., LIU, S. S. & SWINNEY, H. L. 1986 Flow regimes in a circular Couette flow system with independently rotating cylinders. *J. Fluid Mech.* **164**, 155–183.

BANDYOPADHYAY, P. R. 1986 Aspects of the equilibrium puff in transitional pipe flow. *J. Fluid Mech.* **163**, 439–458.

BATCHELOR, G. K. 1969 Computation of the energy spectrum in homogeneous turbulence. *Phys. Fluids Suppl.* II, 233–239.

BENZI, R., PALADIN, G., PARISI, G. & VULPIANI, A. 1985 Characterisation of intermittency in chaotic systems. *IBM Rome Scientific Centre Rep.* G513-4066.

BENZI, R., PATARNELO, S. & SANTANGELO, P. 1987 On the statistical properties of two-dimensional decaying turbulence. *Europhys. Lett.* **3**, 811–818.

CANTWELL, B. J. 1981 Organized motion in turbulent flow. *Ann. Rev. Fluid Mech.* **13**, 457–515.

COLES, D. 1965 Transition in circular Couette flow. *J. Fluid Mech.* **21**, 385–425.

DEAN, R. B. 1976 Reynolds number dependence of skin friction and other bulk flow variables in two-dimensional rectangular duct flow. *Trans. ASME* I: *J. Fluids Engng* **100**, 215–223.

DEVILLE, M., KLEISER, L. & MONTIGNY-RANNOU, F. 1984 Pressure and time treatment for Chebyshev spectral solution of a Stokes problem. *Intl J. Numer. Methods Fluids* **4**, 1149–1163.

GOTTLIEB, D. & ORSZAG, S. A. 1977 *Numerical Analysis of Spectral Methods*, p. 119. Philadelphia: SIAM.

GUCKENHEIMER, J. & HOLMES, P. 1983 *Nonlinear Oscillations Dynamical Systems and Bifurcations of Vector Fields*. Springer.

HENSHAW, W. D., KREISS, H. O. & REYNA, L. G. 1989 On the smallest scales for the incompressible Navier–Stokes equations. *J. Theor. Comput. Fluid Mech.* **1**, 1–32.

HERBERT, T. 1976 Periodic secondary motions in a plane channel. In *Proc. 5th Intl Conf. on Numerical Methods in Fluid Dynamics* (ed. A. I. Van de Vooren & P. J. Zandbergen), pp. 235–240. Springer.

HERBERT, T. 1983 Secondary instability of plane channel flow to subharmonic disturbances. *Phys. Fluids* **26**, 871–874.

JIMÉNEZ, J. 1987 Bifurcations and bursting in two dimensional Poiseuille flow. *Phys. Fluids* **30**, 3644–3646.

JIMÉNEZ, J. 1989 Bifurcations in Poiseuille flow and wall turbulence. In *Fluid Dynamics of 3D Shear Flows and Transition, AGARD-CP* **438**, pp. 14.1–14.11.

JIMÉNEZ, J., MOIN, R., MOSER, R. & KEEFE, L. 1988 Ejection mechanisms in the sublayer of a turbulent channel. *Phys. Fluids* **31**, 1311–1313.

KEEFE, L., MOIN, P. & KIM, J. 1987 The dimension of an attractor in turbulent Poiseuille flow. *Bull. Am. Phys. Soc.* **32**, 2026.

KIM, J., MOIN, P. & MOSER, R. 1987 Turbulence statistics in fully developed channel flow at low Reynolds number. *J. Fluid Mech.* **177**, 133–166.

KRAICHNAN, H. R. 1967 Inertial ranges in two dimensional turbulence. *Phys. Fluids* **10**, 1417–1423.

ORSZAG, S. A. 1971 Numerical simulation of incompressible flows with simple boundaries. I. Galerkin (spectral) representations. *Stud. Appl Maths.* **50**, 293–327.

ORSZAG, S. A. & PATERA, A. T. 1983 Secondary instability of wall bounded shear flows. *J. Fluid Mech.* **128**, 347–385.

POMEAU, Y. 1986 Front motion, metastability and subcritical bifurcations in hydrodynamics. *Physica* **23D**, 3–11.

PUGH, J. D. 1987 Finite amplitude waves in plane Poiseuille flow. Ph.D. thesis, Caltech, Pasadena.

ROZHDESTVENSKY, B. L. & SIMAKIN, I. N. 1984 Secondary flows in a plane channel: their relationship and comparison with turbulent flows. *J. Fluid Mech.* **147**, 261–289.

RUBIN, Y., WYGNANSKI, I. & HARITONIDIS, J. H. 1980 Further observations on transition in a pipe. In *Laminar–Turbulent Transition* (ed. R. Eppler and H. Fasel), pp. 17–26. Springer.

SAFFMAN, P. G. 1971 On the spectrum and decay of random two dimensional vorticity distributions at large Reynolds numbers. *Stud. Appl. Maths.* **50**, 377–383.

SAFFMAN, P. G. 1983 Vortices, stability and turbulence. *Ann. N.Y. Acad. Sci.* **404**, 12–24.

STEWARTSON, K. & STUART, J. T. 1971 A nonlinear stability theory for a wave system in plane Poiseuille flow. *J. Fluid Mech.* **48**, 529–545.

THUAL, O. & FAUVE, S. 1988 Localized structures generated by subcritical instabilities. *J. Phys. Paris* **49**, 1829–1833.

VAN ATTA, C. 1966 Exploratory measurements in spiral turbulence. *J. Fluid Mech.* **25**, 495–512.

VASTANO, J. A. & KOSTELICH, E. J. 1986 Comparison of algorithms for determining Liapunov exponents from experimental data. In *Dimensions and Entropies in Chaotic Systems* (ed. G. Mayer-Kress), pp. 100–107. Springer.

WOLF, A., SWIFT, J., SWINNEY, H. L. & VASTANO, J. 1985 Determining Liapunov exponents from a time series. *Physica* **16D**, 285–317.

WYGNANSKI, I. J. & CHAMPAGNE, F. H. 1973 On transition in a pipe. Part 1. The origin of puffs and slugs and the flow in a turbulent slug. *J. Fluid Mech.* **59**, 281–335.

WYGNANSKI, I. J., SOKOLOV, M. & FRIEDMAN, D. 1975 On transition in a pipe. Part 2. The equilibrium puff. *J. Fluid Mech.* **69**, 283–304.

ZAHN, J. P., TOOMRE, J., SPIEGEL, E. A. & GOUGH, D. O. 1974 Nonlinear cellular motions in Poiseuille channel flow. *J. Fluid Mech.* **64**, 319–345.